Greenland Ice Sheet Ice Slab Expansion and Thickening

Nicolas Jullien[1], Andrew Jachnik Tedstone[1], Horst Machguth[1], Nanna B. Karlsson[2], and Veit Helm[3]

[1]University of Fribourg
[2]GEUS
[3]Alfred Wegener Institute

January 9, 2023

Abstract

We use airborne accumulation radar data acquired over the Greenland Ice Sheet between 2002 and 2018 to identify changes in ice slab extent and thickness. We show that ice slabs several metres thick were already present at least as early as 2002. Between 2012 and 2018, they expanded 13,400-17,600 inland, or by 37-44%. Our results document that the extremely warm summer of 2012 produced near-surface ice layers at higher elevations, enabling ice slabs to develop in locations with only moderate melting in the following summers. With repeated flights over a transect in southwest Greenland, we show that ice slabs can thicken from above and on their undersides. Moderate melting primarily thickens ice slabs by top-down accretion, while large melting events can also trigger ice accretion below the slabs.

[Geophysical Research Letters]

Supporting Information for

Greenland Ice Sheet ice slab expansion and thickening

N. Jullien[1], A. J. Tedstone[1], H. Machguth[1], N. B. Karlsson[2], V. Helm[3]

[1]Department of Geosciences, University of Fribourg, Fribourg, Switzerland

[2]Geological Survey of Denmark and Greenland, Copenhagen, Denmark

[3]Alfred Wegener Institute, Helmholtz Centre for Polar and Marine Sciences, Bremerhaven, Germany

Contents of this file

Introduction

In the following we provide additional information on the processing and interpretation of accumulation radar data in 2002-03 and 2010-18. We provide additional figures that are discussed in the main manuscript as well as in text S1, S2, S3 and S4.

Text S1. Ice content identification in 2002-2003

Dataset preparation

We downloaded all accumulation radar (AR) data acquired over the GrIS. We added coordinates to each radargram by matching the timestamps from the radargram with those provided in the flight path dataset. Radargrams were detrended in the logarithmic domain by the provider (J. Paden, personal communication 2020). We refer to the data in the radargrams as 'signal strength', in the unit of decibels.

Surface picking

We picked the ice sheet surface following the approach used by MacFerrin et al. (2019). First, we manually identified the surface at the start of each radargram. Then, for each trace in the radargram, the surface identification uses a vertical 100-pixel 3-standard deviation pseudo-Gaussian kernel mask over a 40 vertical pixels search window (150 vertical pixels search window in MacFerrin et al. (2019)), centered on the proposed surface. The identified surface of that trace corresponds to the index of the largest value from the convolution between the kernel mask and the radar signal in the search window. The index of the identified surface is then used as a suggested surface in the next trace, and so on until the end of the radargram is reached. When the algorithm failed to identify the surface then we picked the surface manually. The surface picking procedure was smoothed similarly to MacFerrin et al. (2019) by comparing the surface slope in each trace with the average surface slope of the 10 preceding traces. If the slope difference was larger than 5 vertical pixels or was 50% higher than the average slope of the 10 preceding traces, we considered the 20 traces ahead and found the trace whose slope is within 10% the mean slope of the 10 preceding traces. We then calculated the surface location by linear interpolation between the surface pixel before the jump and the next matching trace. We inspected all resulting surface picks manually.

As the firn column is considered to be dry during the springtime airborne radar campaigns, we used the speed of the electromagnetic signal through refrozen ice within firn derived by MacFerrin et al. (2019) to retrieve depth in each radargram. For further

details on the discussion of the speed of the electromagnetic signal in such a medium, we refer the reader to MacFerrin et al., (2019).

Ice content identification

We identified ice content via expert manual classification of the uppermost 30 m of each radargram. Each radargram was inspected using a histogram stretch between the 2.5% and 97.5% percentiles of the radar signal strength distribution from all the radargrams of the corresponding year. As these data have been detrended in the logarithmic domain we are limited to quantifying ice layer and slab extent only, leaving thickness estimates possible only occasionally.

Depending on the surface regime (i.e. ablation zone, percolation zone, dry snow zone), different characteristic features can be identified within the subsurface. Fig. 1 shows four radargrams (0-30 m) that represent different subsurface conditions. Radar returns in the ablation zone (Fig. 1b) are uniform with no major variations in signal strength. The percolation zone can show thin and sharp layering probably associated with decimeter-scale ice layers (Fig. 1c), but can also show meters-thick layering probably associated with ice slabs (Fig. 1d). The dry snow zone shows regular parallel layering associated with annual snow accumulation (Fig. 1e).

We considered whether the signal in Fig. 1c,d was indicative of ice content. Besides ice content, there are two other possibilities: (1) liquid water presence, and (2) wind-hardened, buried surface layers. To check the likelihood of these two other possibilities, we focus on a candidate radargram in SW Greenland (Fig. S1, similar to the one shown in Fig. 1d) where layers several meters thick are thought to correspond to ice. Liquid water was discounted as the return signal associated with liquid water shows typically a mirroring (peak on the opposite side) of the signal compared to the signal peak related to the surface (e.g. Fig. 18 in Karlsson et al. (2019)). This was not observed in the candidate radargram (Fig. S1b-e). Furthermore, liquid water would blind the radar signal below, but we do not see any evidence of this (Figs. 1d and S1b-e).

To investigate the possibility of a wind-hardened buried surface layer, we estimated the thickness of annual snowpack accumulation. Fettweis et al. (2020) indicate that mean annual snowfall ranges between 200 and 600 $\mathrm{mm\ w.e.\ year^{-1}}$ with a spread of 0-150 $\mathrm{mm\ w.e.\ year^{-1}}$ in the area of interest. This gives a low and high end of yearly snowfall of 50-750 $\mathrm{mm\ w.e.\ year^{-1}}$. Considering a firn density of 500 $\mathrm{kg \cdot m^{-3}}$ (Braithwaite et al., 1994) yields a plausible range of 0.1 to 1.5 m thickness for each buried surface layer. As the layers in the radargram are several meters thick it is therefore unlikely that the signal corresponds to a wind-hardened buried layer and so we conclude that the return signal is associated with ice slabs. We interpret thinner layers as indicative of ice layers (see thin layering in Fig. 1c).

Text S2. Ice content identification from 2010 to 2018

With radar data acquired during 2010 to 2018 we had two goals: first, to identify changing ice slab extent for comparison to the extents found in the 2002-03 period, and second, to quantify changes in slab thickness. This second goal required us to be able to quantitatively compare successive radargrams, necessitating a rigorous semi-automated approach to ice content identification.

Dataset preparation

We identified ice slabs in the L1B radargrams collected by the Accumulation Radar (AR) within NASA's Operation IceBridge following a similar approach to MacFerrin et al. (2019). We reprocessed the same 2010-2014 data as were used by MacFerrin et al. (2019). To identify ice slabs in data acquired during 2017 and 2018, we applied a location-based matching between the new radargrams and the 2010-2014 ice slabs extent found by MacFerrin et al. (2019). We retained all coincident radargrams as well as the ones in the vicinity of the ice slabs extent to ensure any changes in the subsurface firn near the pre-existing ice slabs would be identified. We applied a logarithmic transformation to the L1B radargrams (but did not multiply it by 10 as in Carl et al., (2011)) and refer to this as the 'signal strength' of the radargram, in the unit of decibels.

Surface picking and defining exclusions

From the log-transformed radargrams we picked the surface of the ice sheet following the approach used by MacFerrin et al. (2019) (Fig. S2a) . For 2017-2018 data, we manually identified the surface of the ice sheet at the start of each radargram and provided it to the algorithm. We then applied the surface pick to the radargram (Fig. S2b) and extracted the uppermost 100 m in order to carry out the corrections procedure outlined in the next step. We manually excluded areas with lakes and other obvious artefacts (i.e. signal failure) (Fig. S2c).

Correction for aircraft roll and signal attenuation with depth

We corrected the radar signal strength for the roll of the aircraft following MacFerrin et al. (2019) (Fig. S2d). On occasion, the roll correction failed, which was noticeable by

signal return strengths remaining much lower than following a successful roll correction. Such data were excluded from further analysis. In addition, much of the data collected in 2018 were affected by a periodicity artefact caused by the radar beam being steered off nadir during data collection (J. Li, personal communication, 2021) which prevented roll correction and made them ineligible for further analysis.

To ensure that radar signal strength returned from the subsurface would be comparable between radargrams, we subtracted the average surface radar signal strength from the sub-surface signal, thereby removing the majority of the atmospheric influences upon the return signal (Fig. S2e) while retaining the physical dimension of the radar signal. Finally, we corrected for depth attenuation of the radar signal following a slightly modified version from MacFerrin et al. (2019) (we did not apply variance normalisation) (Fig. S2f), and clipped each radargram to the uppermost 30 m corresponding to the depth range which is expected to contain ice slabs in order to simplify later processing steps.

Re-scaling of radar signal

Fourteen of the 448 radargrams (3%) displayed little variation in their return signal, making it difficult to identify ice slabs. We therefore rescaled these depth-corrected radargrams by applying a histogram stretch using the 5^{th} and 95^{th} percentiles from the combined distribution of the other depth-corrected radargrams.

Initial comparison with MacFerrin et al., (2019)

Initially, we reprocessed the 2010-14 data using the same ice identification algorithm as MacFerrin et al. (2019). They used a relative threshold unique to each radargram to identify ice slabs in the uppermost 20 m, but we found that this approach did not reliably return identical ice features between individual successive radargrams. Hence, the original algorithm is not well-suited to compare ice thickness across individual years. We therefore developed a new algorithm to identify ice slabs in the uppermost 20 m, based on the application of a universal range of radar signal strengths extracted from a reference radargram.

143 Identification of ice content versus porous firn

144 **Identifying the return signal strength that is indicative of ice content.** We aimed to
145 identify the range of radar signal strengths that enables differentiation between porous
146 firn versus ice content across the entire dataset. In 2013, MacFerrin et al. (2019) collected
147 in-situ ground penetrating radar data and firn cores coincident with an Operation
148 IceBridge AR radargram during the same spring, which they used to validate the
149 identification of ice slabs in airborne radar data. Here, we adopt this AR radargram as our
150 "reference radargram" (see Fig. S3a).

151 We manually identified ice slabs in the depth-corrected AR reference radargram (Fig.
152 S3b), referred as in-situ ice content. We adopted a conservative approach, seeking to
153 include ice which was positively identified in ground-based in-situ GPR data by
154 MacFerrin et al., (2019), easily distinguishable from porous firn, and continuous. Next, we
155 used this mask to extract the distributions of signal strength from the reference
156 radargram for (a) porous firn and (b) ice content (Fig. S4). The overlap in the signal return
157 strength between the two facies means that a single threshold to fully differentiate
158 porous firn and ice content cannot be defined. Instead, we developed an algorithm using
159 a range of thresholds based on the quantiles of the ice content signal distribution to
160 distinguish between ice content and porous firn.

161 Fig. S3c illustrates the performance of the new algorithm on the reference radargram in
162 detecting ice content for quantile 0.65 of the ice content distribution (our lower
163 threshold), and Fig. S3d for quantile 0.79 (our upper threshold). Quantile 0.65 is the
164 highest quantile for which the algorithm correctly identifies ice without erroneously
165 including firn (see Tab. S1), at the cost of missing some ice content (see Fig. S3c). Above
166 this threshold, some areas that have been mapped to be porous firn start to be falsely
167 identified as ice. These facies correspond to an intermediate state between porous firn
168 and ice slabs (see Fig. 2b,c in MacFerrin et al. (2019)), most likely several ice layers within
169 firn. By quantile 0.80 (not shown), porous firn unlikely to contain numerous ice layers
170 starts to be identified as ice. We therefore applied thresholds in the quantile range 0.65

to 0.79 from the ice content distribution to detect ice presence. We discuss accuracy further below.

Extracting ice content. For each radargram, we extracted ice content across the range of thresholds described above in 0.01 increments, corresponding to retrievals at 15 individual thresholds. Following MacFerrin et al. (2019), we removed small-scale noise by applying a filter to each ice content retrieval to remove small individual ice features 1-2 pixels wide, and a continuity threshold to retain only pixels which were spatially continuously connected to at least 350 other pixels. We show the resulting ice content identification for quantile 0.65 in Fig. S2h and quantile 0.79 in Fig. S2i. The ice features identified in each individual quantile is referred to ice slabs.

Ice content likelihood. We computed an ice content likelihood for each radargram as the percentage of the 15 different levels of ice content in which each pixel was identified as containing ice (Fig. S2g).

Post-processing and verification. In some radargrams we found that some porous firn areas were wrongly identified as ice, probably because of the significant overlap of the two distributions (Fig. S4). We therefore manually excluded these areas from the final results (Fig. S2j). The list of exclusions is provided in the code repository.

Accuracy assessment

We considered the accuracy of the extreme end members of the quantile range (quantile 0.65 and quantile 0.79). Tables S1 and S2 show the two contingency tables given by quantiles 0.65 and quantile 0.79 with respect to the in-situ ice content. As could be expected from the ice content and porous firn signal strength distributions (Fig. S4), a lower threshold quantile performs better in correctly identifying porous firn but performs less well in correctly identifying ice. Conversely, a higher threshold quantile performs better in identifying ice compared to a lower threshold but at the cost of a poorer performance in correctly identifying porous firn. Overall, the total accuracy is higher for the highest quantile.

Ice slab extent

As described in the main text, we defined ice slabs as present in areas with at least 1 m of subsurface ice content by the end of the study period. Following MacFerrin et al. (2019), we only mapped ice slabs above the long-term ELA (i.e. where firn exists), and so our lower ice slabs bounds match theirs.

Final comparison with MacFerrin et al. (2019)

At higher elevations, our ice slab identification yielded some differences with the identification by MacFerrin et al. (2019). Indeed, inspection of individual radargrams revealed that MacFerrin et al. (2019) incorrectly identified ice slabs in some areas, especially in the NE towards the high boundary. As a result, our final ice slab extent differs slightly from MacFerrin et al. (2019). The largest differences are found in the NW, NO and NE (Fig. S12). For example, our 2010-2018 upper ice slabs limit extends less inland compared to the 2010-2014 extent from MacFerrin et al., (2019) in-between upstream of Petermann glacier and Qaanaaq Mitarfik (Thule Air Base) in the NW and NO. The similar is observed upstream of Nioghalvfjerdsbrae (79 N Glacier) in the NE. Overall, MacFerrin et al., (2019) estimated ice slabs extended over 64’800-69’400 km^2 in 2014; we find ice slabs extended over 60’400-73’500 km^2 in 2018.

Text S3. Distinction between, 'in-initiation', 'in-development' and 'well-developed' ice slabs

We analyze the ice content change from the start to the end of the studied period. We identify three stages in ice slab development corresponding to their changes in thickness:

i. In the 'in-initiation' stage, the firn was free of ice slabs at the start of the studied period, and had developed new ice slabs by the end of the studied period.

ii. In the 'in-development' stage, ice slabs experienced substantial (metres) thickening during the studied period.

iii. In the 'well-developed' stage, the thickness of the ice slab was already large (i.e. larger than 10 m thick) at the start of the studied period; its thickness often increased further during the studied period.

In Fig. S5 we illustrate these different categories by splitting transect F (Fig. 3f) into corresponding sectors. Note that we did not set the maximum boundary of ice thickness to be 16m for this analysis; ice thickness can thus reach 20 m.

In the "well-developed" sector, the median ice content stayed roughly the same in 2017 compared to 2010 (14 m and 15 m respectively) (Fig. S5b), with negligible overall change (-2% in 2017 compared to 2010) (Fig. S5e).

In the "in-development" sector, the median ice content increased from 4.2 m to 11.5 m (Fig. S5c, see also the quantiles 0.25 and 0.75 in Table S3), equivalent to an increase of 194% from 2010 to 2017 (Fig. S5f).

In the "in-initiation" sector, no ice slab was identified in 2010, but a new ice slab had developed by 2017 (Fig. S5g) whose median ice content was 5 m in 2017 (Fig. S5d).

We performed the same analysis for transects C and D (Fig. 3c,d) and we present the results in Table S3. We conclude similar patterns as in transect F are taking place in transects C and D.

Text S4. Ice accretion

We differentiate between top-down ice accretion versus accretion on the undersides of ice slabs (Fig. 4d). From spring 2012 to spring 2018, both top-down and underside accretion took place, which is clearly identifiable once it has been separated from lateral and vertical displacement of the ice slab.

(i) **Lateral displacement:** Using local surface velocities measured from 2009 to 2013, we estimate that the ice was displaced laterally by ~312 m (Doyle et al., (2014)). This agrees well with the ~360 m that we estimate by comparing the distribution of ice content located between 15.93 and 16.52 km in 2012 with its corresponding location in 2018.

(ii) **Vertical displacement:** The bottom of the "double-layered" ice slab (from 13.8 to 15.6 km) in 2012 was found to be roughly 2.6 m lower by 2018, while the ice slab from 16.5 to 17.7 km was found 3m deeper (Fig. 4d). This apparent movement is due to subsequent accumulation. We estimated the burial of the ice slab bottom from 2012 to 2018 using ice cores collected previously (Rennermalm et al., (2021)). Due to extreme melting in summer 2012 (Fig. S6), the ice slab surface was exposed (Machguth et al., 2016), meaning that any firn pore space remaining from 2011-12 accumulation was minimal or non-existent. We were therefore able to estimate the lower boundary of the ice slab at KAN_U in 2013 and 2017, concluding that the bottom of the thick ice slab that developed in summer 2012 was buried by roughly 1.7 m from 2013 to 2017. We lack cores from 2018 and thus cannot estimate potential firn replenishment from spring 2017 to spring 2018. Nevertheless, this estimate of 1.7 m burial between 2013 and 2017 seems a reasonable lower bound approximation for 2012-2018 firn replenishment.

(iii) **Top-down accretion** took place on top of the slab, thickening the ice slab by 2.9 m from 2012 to 2018 in-between 16.5 and 17.7 km (Fig. 4d).

(iv) **Ice accretion on the undersides of ice slab** also occurred between 2012 and 2018 between 13.8 and 15.6 km, commencing at 11-13 m below the surface and extending to 20 m deep (Fig. 4d).

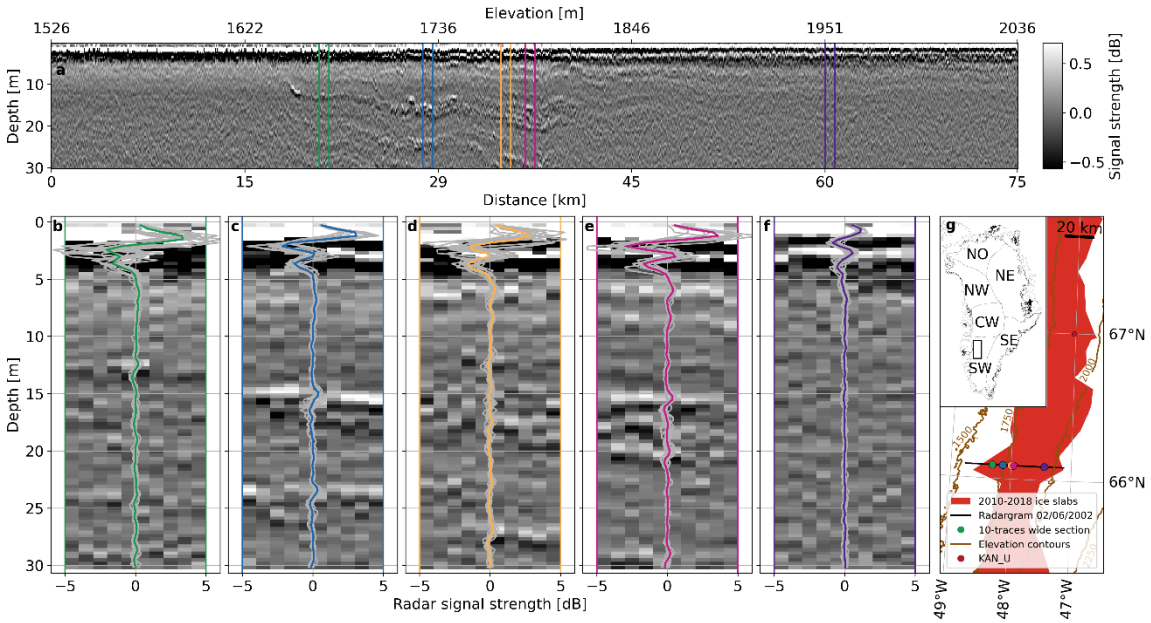

272

273 **Figure S1. Examples of ice content in 2003-03 data.** (a) Radargram acquired in SW
274 Greenland on June 2nd, 2002 (background) and 10-traces wide limits of radar signal
275 strength with color coding corresponding to panels b-f. (b-f) Individual trace signal
276 profile (grey lines), average over the 10 traces of interest (color), and 10-traces
277 radargram on the background. (b) An ice layer at 12-13 m depth. (c) Ice slabs are present
278 between 14 m and 17 m depth and between 23 m and 25 m depth, (d) between 10 m
279 and 20 m depth and at 27m depth, (e) in-between 15-21 m depth as well as at 29 m
280 depth. (f) Porous firn without ice layers nor slabs. (g) Location of radargram compared to
281 2010-2018 ice slabs extent.

282

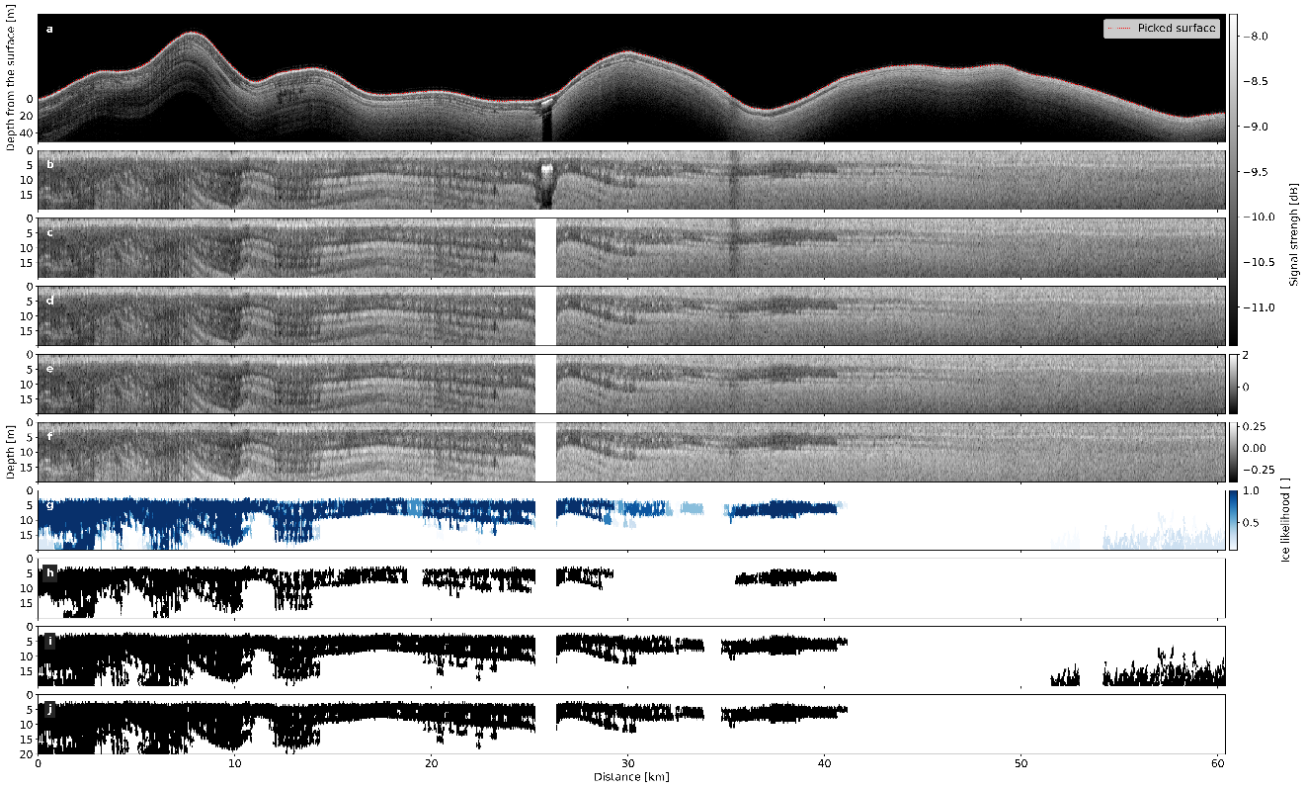

283

284 **Figure S2. Processing steps to identify ice content from airborne accumulation**
285 **radar data**, illustrated using radargram 20140416_05_007_009. (a) raw airborne
286 accumulation radar (AR) data before surface identification with the identified surface (red
287 dotted line). (b) AR data after surface picking. (c) AR data after screening for areas to be
288 excluded. (d) AR data after correction for the roll of the aircraft. (e) AR data after the
289 removal of the average surface signal strength. (f) AR data after correction for the
290 attenuation of the signal with depth. (g) Ice content likelihood, ranging from 0 to 1. (h)
291 Ice content presence where each cell was mapped as ice at quantile 0.65. (i) Ice content
292 presence where each cell was mapped as ice at quantile 0.79, corresponding to a
293 likelihood of 1. (j) Final ice content at quantile 0.79, following manual porous firn
294 exclusion.

295

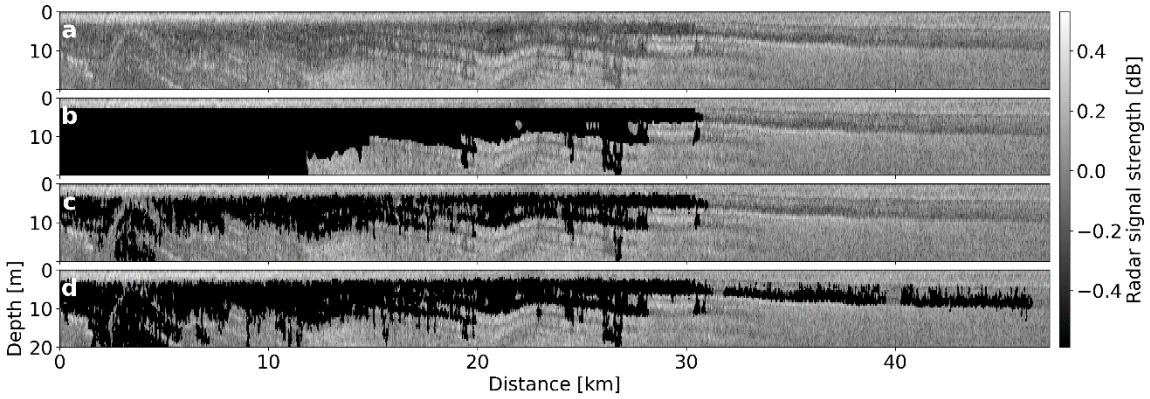

296

297 **Figure S3. Extraction of characteristic radar return strength from reference**
298 **radargram.** (a-d) Depth corrected data for the reference radargram derived from AR
299 data. (b) in-situ ice content mask (black). (c) Ice content retrieval using quantile 0.65 of
300 the ice content distribution signal strength derived by applying the in-situ ice content
301 mask (b) to the data in panel a. (d) As for panel c, using quantile 0.79.

302

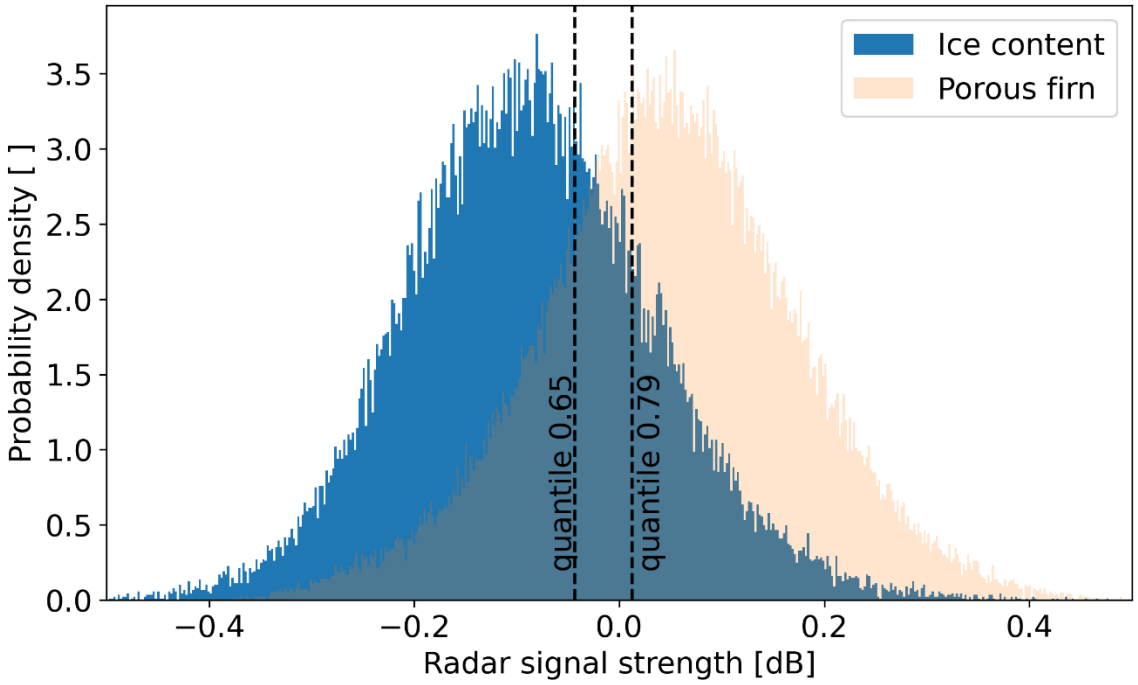

Figure S4. Porous firn versus ice content signal strength distribution. Calculated according to in-situ ice content in the depth-corrected reference radargram. The vertical dashed lines correspond to the quantile 0.65 and quantile 0.79 of the ice content distribution.

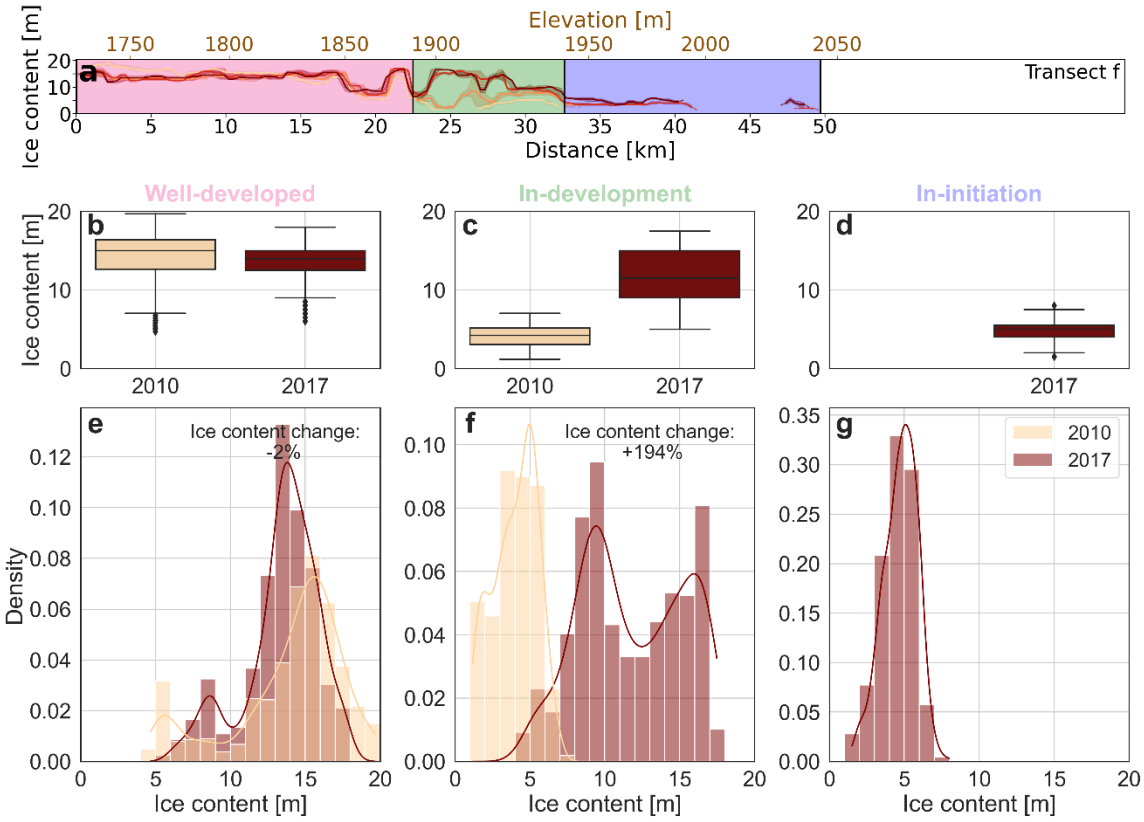

Figure S5. Ice content change along transect F. (a) Ice content change from 2010 to 2017 (colored lines, same as in Fig. 3f) along the transect. The different sectors of changes in ice slabs thickness are indicated by the background shading: well-developed (pink), in-development (green), in-initiation (blue). (b-d) Boxplot of ice content in 2010 and 2017 in the three sectors. (e-f) Distribution of ice content in 2010 and 2017 in the three sectors. Lines denotes the kernel density estimate of the distributions. Percentage change indicate the relative change in total ice content in the sector of interest in 2017 compared to 2010.

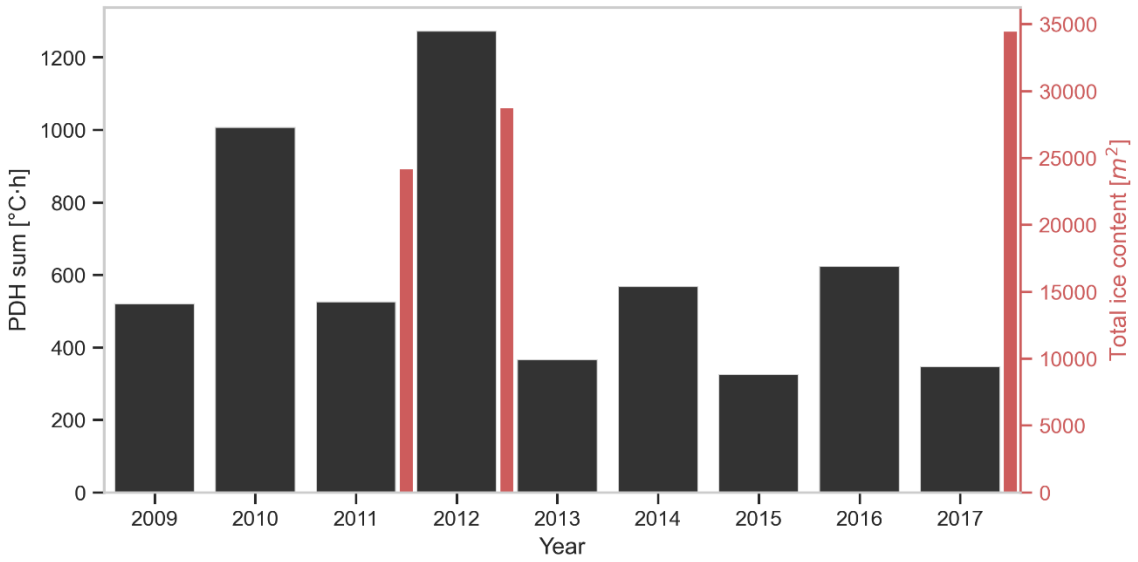

Figure S6. Melt potential at KAN_U. Positive Degree Hour sum [℃ · h] during each summer (black) and total ice content according to radargrams each spring (red) within the area delimited by thick dashed lines in Fig. 4 (from 13.8 to 17.7 km).

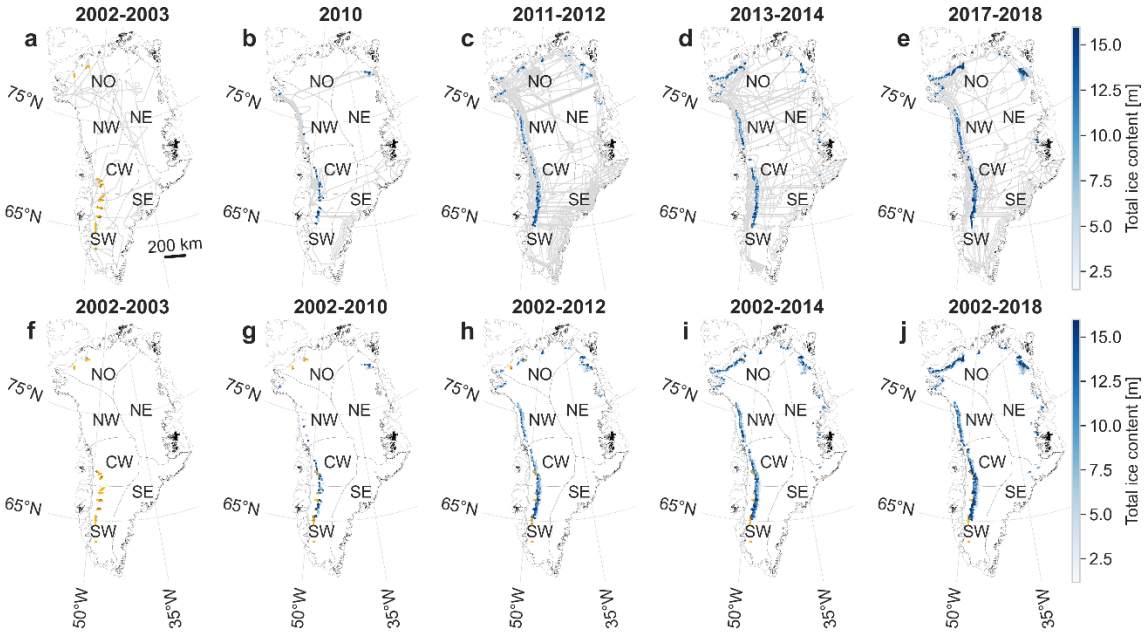

Figure S7. Ice slab mapping and growth over time. (a-e) Ice slabs mapped during each time period (color) and flight line (gray). (f-j) Cumulative ice slabs mapping (color) over successively longer time periods.

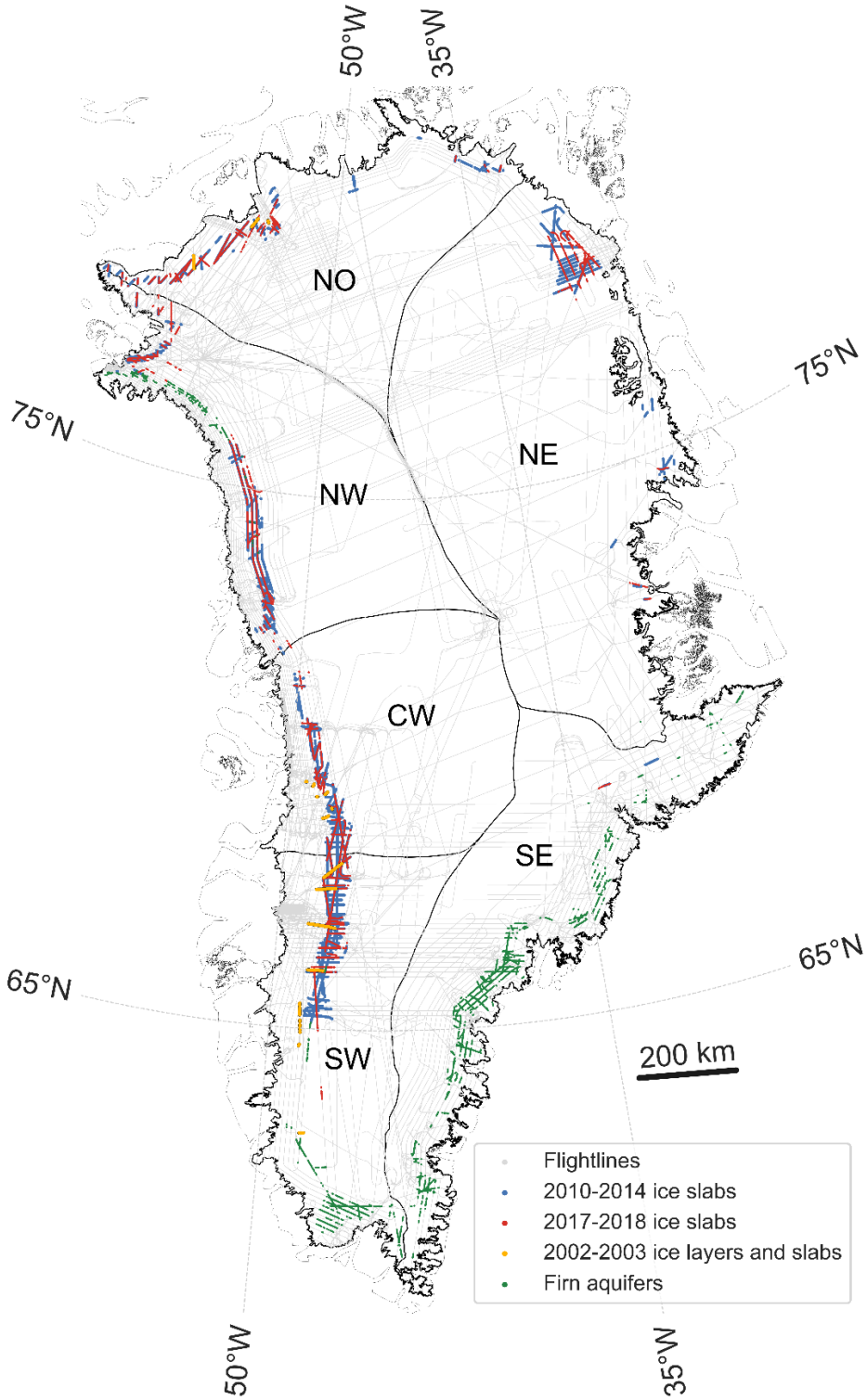

Figure S8. Combined ice slab presence from 2002 to 2018. Ice layers and slabs mapped in 2002-03 (orange), 2010-14 (blue) and 2017-18 (red), firn aquifers in 2010-2014 (Miège et al., 2016) (green). Flight lines associated with 2002-2018 ice slabs are displayed in the background in grey.

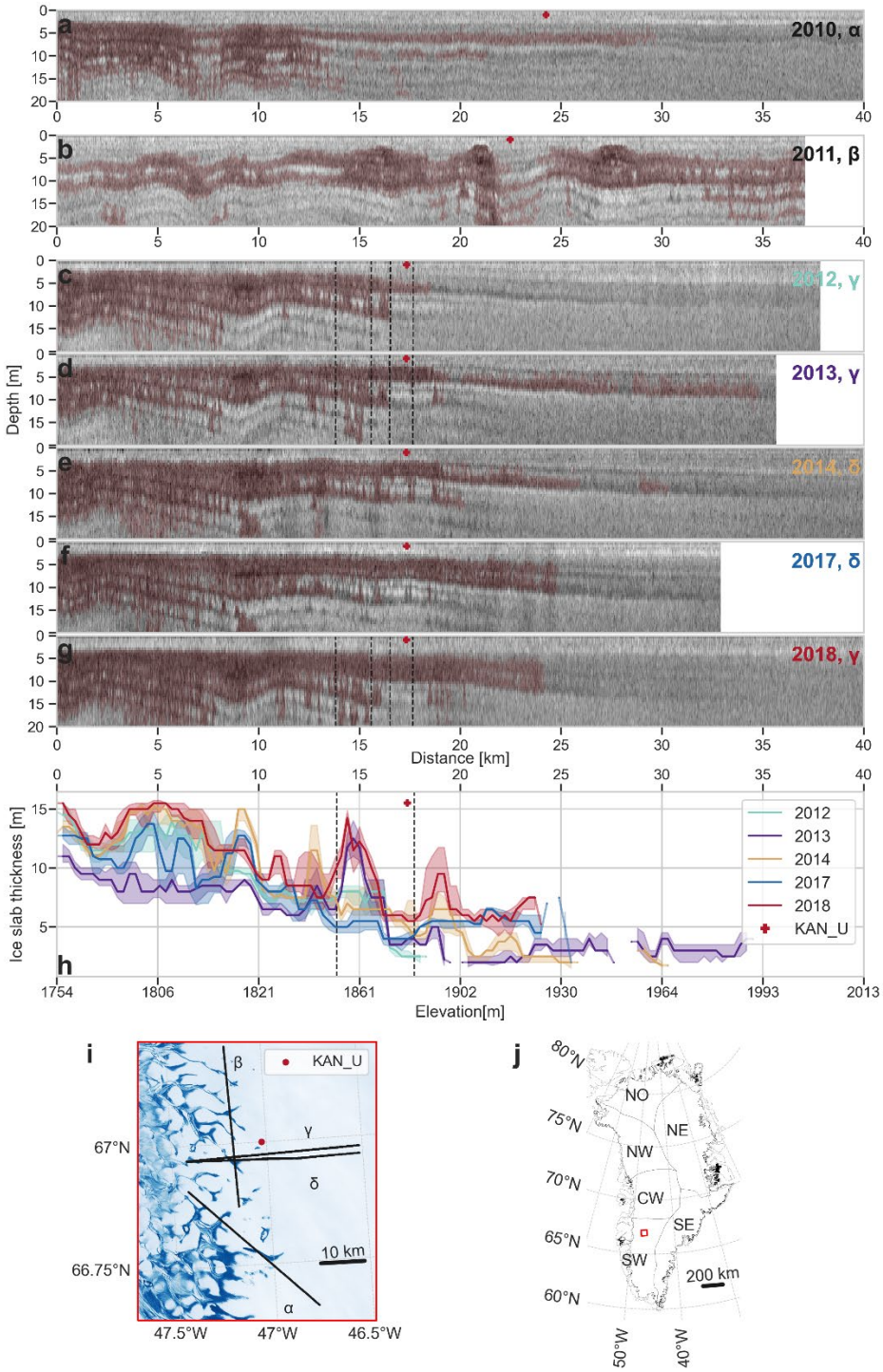

Figure S9. Ice thickness through time along a transect close to KAN_U (red marker in each panel). (a-g) Radargrams in greyscale and resulting maximum likely ice content (quantile 0.79) in red. Dashed vertical lines delineate the areas discussed in the text. (h) Ice slab thickness in uppermost 20 m of radargrams (from 2012 onwards). Equivalent elevation (m above WGS84 ellipsoid) on lower x axis. (i) Near-infrared (band 8) Sentinel-2 image acquired on August 23rd, 2021, with radargram locations. (j) Transect location on the GrIS (red square).

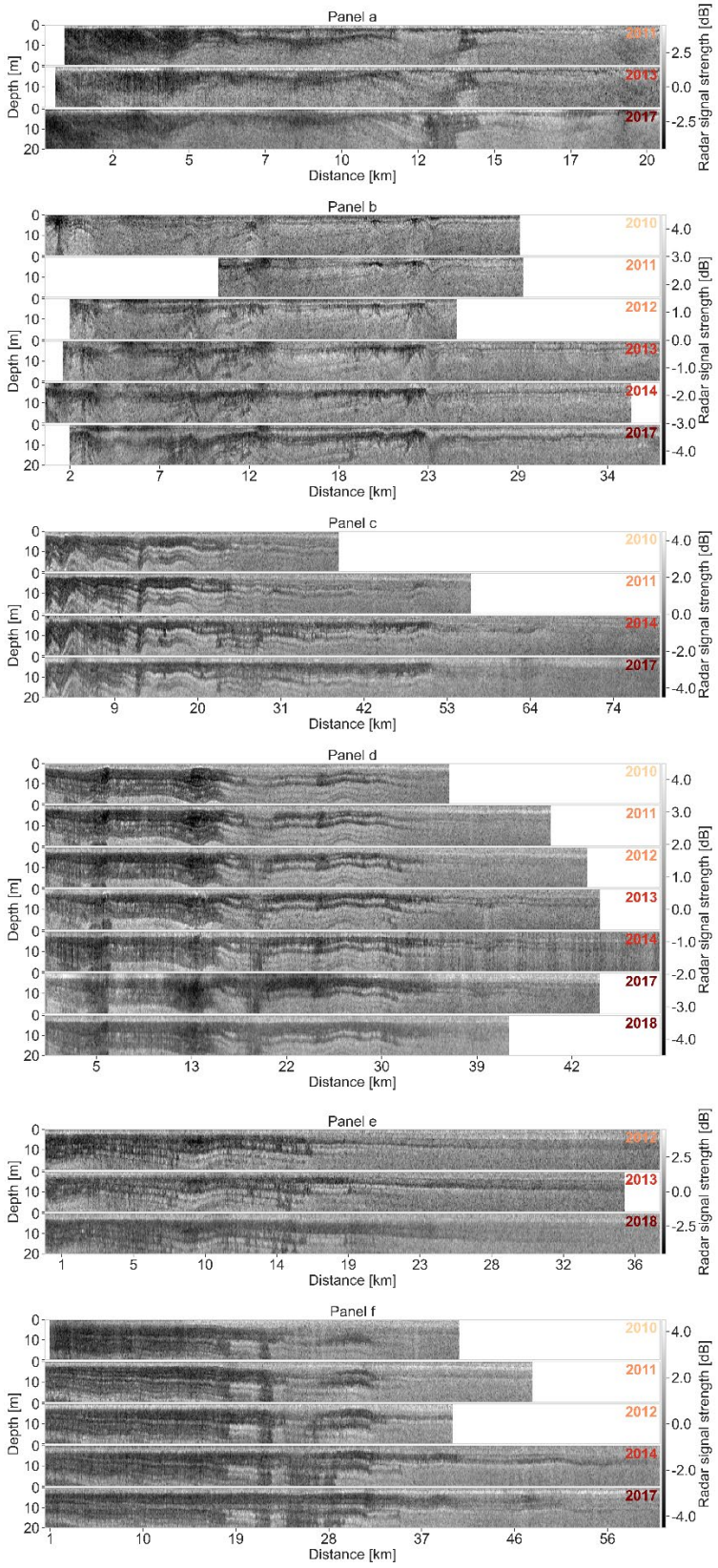

Figure S10. Yearly radargrams of transects used in Fig. 3

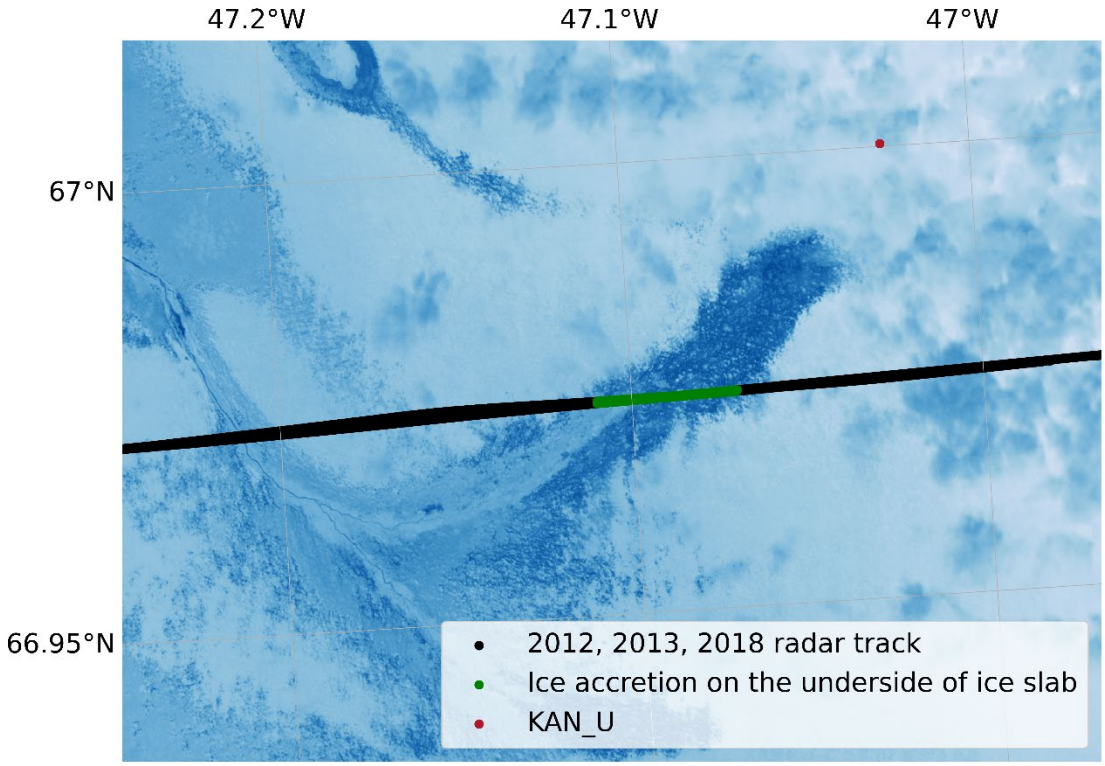

345

346 **Figure S11. Coincident surface hydrology and ice slab accretion.** Near-infrared (band
347 8) Sentinel-2 image acquired on August 24th, 2016. Dark blue corresponds to slush
348 fields. A developed hydrological network is seen in the lower left. Clouds are visible in
349 the upper right. Radargrams (black) acquired in 2012, 2013 and 2018 (same as Fig. 4b,d).
350 Radargrams with ice accretion on the underside of ice slab (green) identified by
351 comparing 2012 with 2013 and 2018 radargrams (13.8 to 15.6 km in Fig. 4). KAN_U is
352 indicated by the red dot.

353

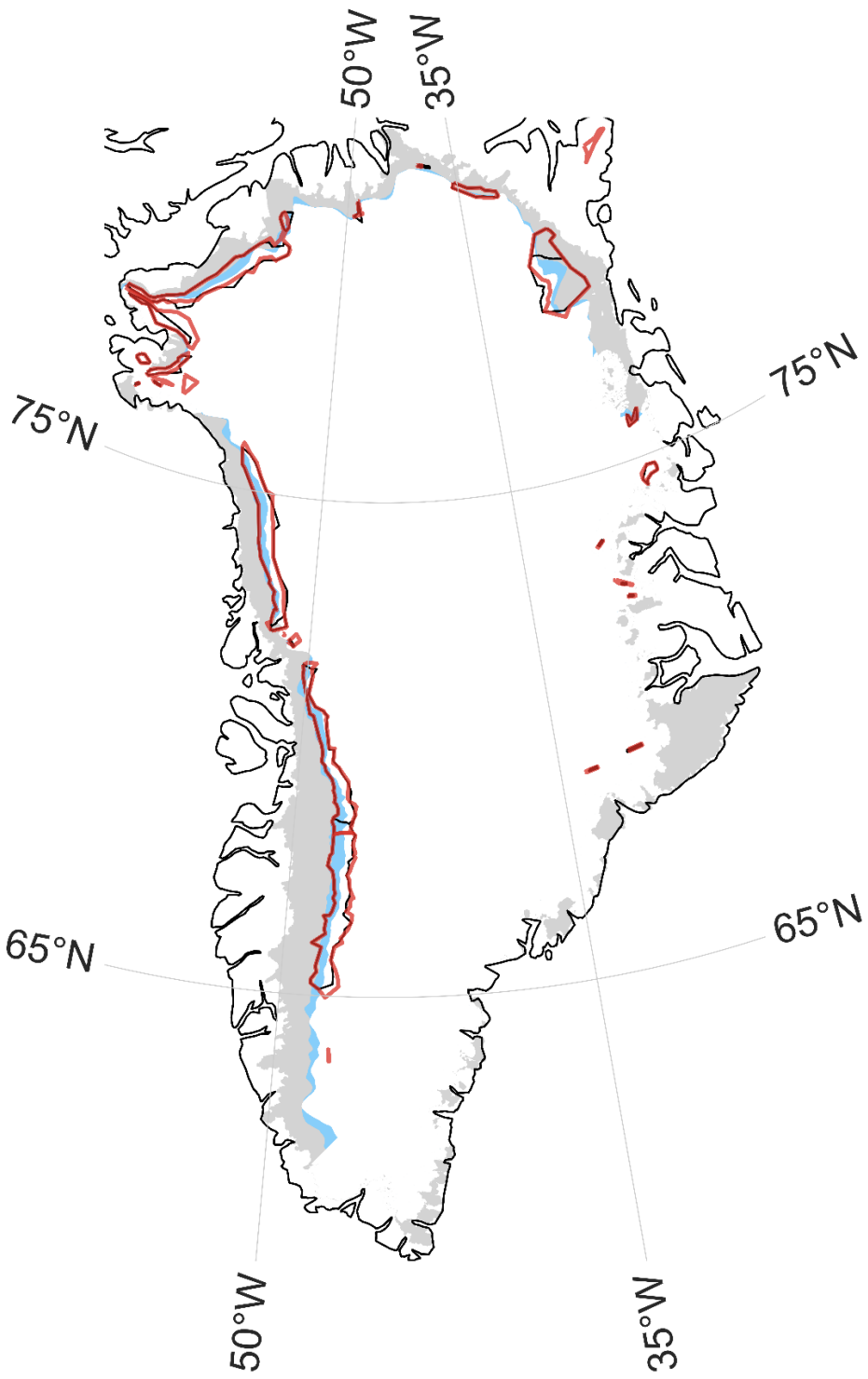

Figure S12. Comparison between visible surface runoff area and ice slab extent. Visible surface runoff area in 1985-1992 (grey shading) and expansion in 2013-2020 (blue shading) from Tedstone & Machguth (2022). Ice slabs extent in 2010-2014 from MacFerrin et al. (2019) (black). Ice slabs extent at quantile 0.79 in 2010-2018 in this study (red).

	Firn (Q 0.65)	Ice (Q 0.65)	Sum	Producer acc.
Firn (in situ)	**98894**	413	99307	99.58%
Ice (in situ)	19426	**21897**	41323	52.99%
Sum	118320	22310	**140630**	
User acc.	83.58%	98.15%		**Overall acc. 85.89%**

Table S1. Contingency table summarizing the performance of the algorithm in correctly retrieving porous firn and ice using quantile 0.65 of the ice content distribution as the threshold differentiating between porous firn and ice compared to the in-situ ice content being the reference. Values are in pixels. The producer's accuracy (producer acc.) relates to omission errors, e.g. not retrieving ice when it is ice, while the users' accuracy (user acc.) relates to commission errors, e.g. retrieving porous firn as ice. The overall accuracy (overall acc.) relates to how well the algorithm performs in correctly retrieving both ice and porous firn compared to the reference radargram.

	Firn (Q 0.79)	Ice (Q 0.79)	Sum	Producer acc.
Firn (in situ)	**92999**	6308	99307	93.65%
Ice (in situ)	11001	**30322**	41323	73.38%
Sum	104000	36630	**140630**	
User acc.	89.42%	82.78%		**Overall acc. 87.69%**

Table S2. As Table S1, using quantile 0.79 of the ice content distribution as the threshold.

	Year	Well-developed		In development		In initiation	
		[$Q_{0.25}$; $Q_{0.5}$; $Q_{0.75}$]	Change	[$Q_{0.25}$; $Q_{0.5}$; $Q_{0.75}$]	Change	[$Q_{0.25}$; $Q_{0.5}$; $Q_{0.75}$]	Change
C	2010	[7.7 ; 10.5 ; 13.6]	**+2%**	[3.7 ; 4.6 ; 5.1]	**+62%**	-	**-**
	2017	[6.0 ; 10.0 ; 15.0]		[5.0 ; 6.5 ; 8.5]		[4.5 ; 5.5 ; 6.0]	
D	2010	[11.5 ; 13.3 ; 15.5]	**+11%**	[2.6 ; 3.5 ; 4.4]	**+101%**	-	**-**
	2018	[12.5 ; 15.0 ; 16.5]		[5.0 ; 6.5 ; 9.0]		[4.5 ; 5.5 ; 6.0]	
F	2010	[12.6 ; 15.0 ; 16.4]	**-2%**	[3.0 ; 4.2 ; 5.1]	**+194%**	-	**-**
	2017	[12.5 ; 14.0 ; 15.0]		[9.0 ; 11.5 ; 15.0]		[4.0 ; 5.0 ; 5.5]	

Table S3. Summary statistics table of ice content on three transects in Fig. 3 (transects C, D, F), for the three stages of ice slab development at the start and end of the studied period. $Q_{0.25}$, $Q_{0.5}$, $Q_{0.75}$ correspond to quantiles 0.25, 0.5 and 0.75 of ice content respectively. The ice content change represents the relative change of ice content by 2017 compare to 2010.

Greenland Ice Sheet Ice Slab Expansion and Thickening

N. Jullien[1], A. J. Tedstone[1], H. Machguth[1], N. B. Karlsson[2], V. Helm[3]

[1]Department of Geosciences, University of Fribourg, Fribourg, Switzerland.

[2]Geological Survey of Denmark and Greenland, Copenhagen, Denmark.

[3]Alfred Wegener Institute, Helmholtz Centre for Polar and Marine Sciences, Bremerhaven, Germany.

Corresponding author: Nicolas Jullien (nicolas.jullien@unifr.ch)

Key Points:

- Ice slabs were already present in the early 2000s in southwest, central-west and north Greenland.
- Ice slabs expanded inland from 2002 to 2018 and thickened by top-down accretion and by accretion on their undersides.
- Near-surface ice layers support subsequent ice slab development.

Abstract

We use airborne accumulation radar data acquired over the Greenland Ice Sheet between 2002 and 2018 to identify changes in ice slab extent and thickness. We show that ice slabs several metres thick were already present at least as early as 2002. Between 2012 and 2018, they expanded 13,400-17,600 km^2 inland, or by 37-44%. Our results document that the extremely warm summer of 2012 produced near-surface ice layers at higher elevations, enabling ice slabs to develop in locations with only moderate melting in the following summers. With repeated flights over a transect in southwest Greenland, we show that ice slabs can thicken from above and on their undersides. Moderate melting primarily thickens ice slabs by top-down accretion, while large melting events can also trigger ice accretion below the slabs.

Plain Language Summary

Above the equilibrium line elevation, seasonal snow is not entirely removed by summer melting. As a result, firn - an interannual layer made of old snow and refrozen meltwater - builds up. Firn holds the potential to buffer sea level rise by trapping liquid water within its pore space. However, surface melting has increased in recent decades, making large quantities of water available to percolate into the firn where it refreezes, eventually creating metres-thick ice slabs that hinder future percolation. We mapped ice slabs in the subsurface firn (0-20m depth) by using airborne radar surveys and show that they have expanded inland and thickened from 2002 to 2018. Once formed, ice slabs continue to thicken, even under moderate melt conditions. Recent increases in the ice sheet's visible runoff area match well with the expansion of ice slabs, so we conclude that ice slabs will be an important control on the future runoff area of the ice sheet.

1 Introduction

In the 1990s, the mass balance of the Greenland Ice Sheet (GrIS) was close to equilibrium, but has been negative for the last two decades (The IMBIE Team, 2020). Iceberg calving rates increased (King et al., 2020; Rignot et al., 2008; The IMBIE Team, 2020) and the surface mass balance (SMB) has decreased as a result of increasing melt and runoff (Enderlin et al., 2014; Fettweis et al., 2017; The IMBIE Team, 2020; van den Broeke et al., 2016). Furthermore, extremely warm summers such as in 2010, 2012, 2016 and 2019 (Mikkelsen et al., 2016;

Tedesco et al., 2011, 2013; Tedesco & Fettweis, 2020) triggered unprecedented surface melt rates at high elevations (Hall et al., 2013; Nghiem et al., 2012) and exceptionally high volumes of runoff (Mikkelsen et al., 2016; van Angelen et al., 2014).

Recent increases in surface melting have densified the subsurface firn (Machguth et al., 2016; Mikkelsen et al., 2016; van Angelen et al., 2014). Firn is found above the equilibrium line and consists of interannual snowpack, the density of which increases by compaction through burial but also due to percolation and refreezing of surface meltwater (Braithwaite et al., 1994; Brown et al., 2011; Pfeffer & Humphrey, 1998). Firn has the potential to trap and store meltwater within its pore space, thereby buffering the GrIS contribution to sea level rise (Harper et al., 2012; Pfeffer et al., 1991).

In the percolation zone, where surface melt rates are substantial but usually do not deplete the seasonal snow completely, the fate of meltwater varies mainly with annual snowfall. Where snowfall rates are high (~1000 +/- 400 mm w.e. per year), mostly in southeast and south Greenland, liquid water percolates to a depth where it forms perennial firn aquifers (Forster et al., 2014; Miège et al., 2016; Miller et al., 2022). Conversely, in regions where accumulation rates are lower and which have recently experienced significant melting, ice slabs several metres thick can form – mostly along the west, north and northeast of the GrIS (MacFerrin et al., 2019; Miller et al., 2022). In these regions, increased meltwater percolation during several successive summers fused centimeters-scale ice lenses into increasingly contiguous ice layers tens of centimeters thick and eventually metres-thick slabs, thereby decreasing the firn's permeability (de la Peña et al., 2015; Vandecrux et al., 2019). Ice slabs form an aquitard, preventing most subsequent meltwater from reaching the relict pore space below (MacFerrin et al., 2019; Machguth et al., 2016).

Ice slabs favour the development of surface streams in the high percolation zone (Machguth et al., 2016; Mikkelsen et al., 2016; Tedstone & Machguth, 2022). The area of the ice sheet drained by surface rivers increased by 29% between 1985 and 2020, corresponding strongly with the locations of ice slabs mapped previously and suggesting that 5-10% of recent ice-sheet-wide mass losses originated from these newly densified parts of the accumulation zone (Tedstone & Machguth, 2022). This underlines that it is essential to understand firn densification and ice slab

development for inclusion in ice sheet mass balance models that are used for projections of future ice sheet runoff (de la Peña et al., 2015). Despite their emerging importance to future runoff magnitude, ice slabs have only been mapped over a short time period: with accumulation radar from 2010 to 2014 (MacFerrin et al., 2019), and through a proxy approach with satellite microwave radiometry from 2015 to 2019 (Miller et al., 2022). Here we investigate changes in the extent and thickness of ice slabs using airborne radar observations acquired during spring-time campaigns between 2002 and 2018.

2 Data and Methods

To map ice layer and slab locations in 2002-03 we used data collected by 600-900 MHz accumulation radar (Kanagaratnam et al., 2004; Lewis, 2010). To examine changing ice content during 2010-18, we used the 550-900 MHz accumulation radar (Carl et al., 2011; CReSIS, 2021; Rodriguez-Morales et al., 2010) ; the 2010-14 data that we processed are identical to those used by MacFerrin et al. (2019).

Data acquired during 2002-03 were detrended in the logarithmic domain by the provider, so they have virtually no radiometric information (J. Paden, personal communication 2020). This means they are only useful for layer tracking. Nevertheless, the radiometric variability of the signal is large enough to enable manual ice identification (Text S1). For radargrams acquired between 2010 and 2018, we developed a semi-automated approach based on MacFerrin et al. (2019) (Text S2). In brief, to prepare the radargrams we picked the ice sheet surface, corrected for the roll of the aircraft, removed the impact of varying atmospheric conditions by subtracting the average surface signal strength, and applied a correction for depth attenuation.

We aimed to detect changes sub-surface ice thickness through time. MacFerrin et al. (2019) used a normalised threshold to detect ice content, but we found that this yielded strong differences between co-located radargrams over successive years (Text S2). Instead, we examined a range of radar signal strengths extracted from a "reference" radargram as thresholds to discriminate between porous firn and ice content in the uppermost 20 m. To determine the appropriate range of radar signal strengths, we first manually digitised ice content in the reference radargram based on comparison with in-situ ground penetrating radar measurements and firn cores acquired by MacFerrin et al. (2019) (Fig. S3). Next, we used our reference radargram to determine the signal

return strength given by (a) ice content versus (b) porous firn. The signal distributions of ice content and porous firn partially overlap (Fig. S4). Following a sensitivity analysis (Text S2), we chose lower and upper signal strength thresholds which correspond to the minimum and maximum likely ice content, respectively. The producer's accuracy (overall accuracy) in detecting ice content is 53% (86%) at the lower threshold and 73% (88%) at the higher threshold (Tables S1, S2). For each radargram we also estimated the likelihood of ice content presence between the lower and upper thresholds when ice is first detected. Thus, 100% ice likelihood corresponds to detection at the lower threshold, while 50% corresponds to detection mid-way between the lower and upper thresholds. Finally, following MacFerrin et al., (2019), we identify ice slabs where radar-detected ice content is at least 1 m thick, and consider them to have a maximum accumulation radar-detected thickness of 16 m. We use the term 'ice layers' to refer to ice content less than ~1 m thick.

As a proxy for surface melting, we calculated Positive Degree Hour sum using a similar approach to degree-day modelling (Hock, 2003), using in-situ 2 m air temperature measurements from 2009 to 2017 at the automatic weather station KAN_U (Fausto et al., 2021). We summed every positive 1-hour average temperature (i.e. above 0°C) for each year.

3 Results

3.1 Ice slab expansion from 2002 to 2018

Ice layers and slabs were present in 2002-03 (Fig. 1, 2a), up to several meters thick in SW Greenland (Fig. 1a,c-d). Although the observations are relatively sparse (Fig. S7a), they were also identified in the CW, in the vicinity of Sermeq Kujalleq's (Jakobshavn Isbrae) high percolation zone. Ice layers and slabs were identified in the NO but not in the NW nor the NE, although spatial coverage was limited in the latter regions.

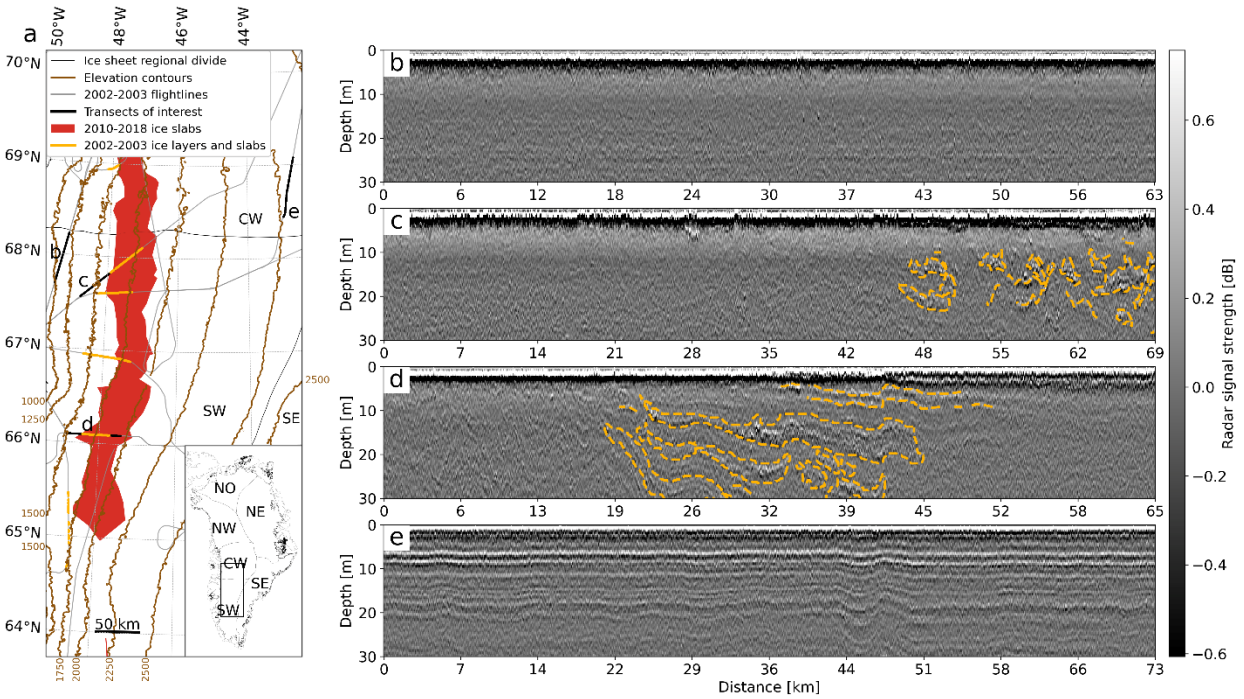

Figure 1. Ice layers and slabs in central and southwest Greenland in 2002-2003. (a) Regional zoom of radargram locations. Radargrams with ice layers/slabs identification overlaid (orange dashed lines) acquired from the (b) ablation zone (c-d) percolation zone and (e) dry snow zone.

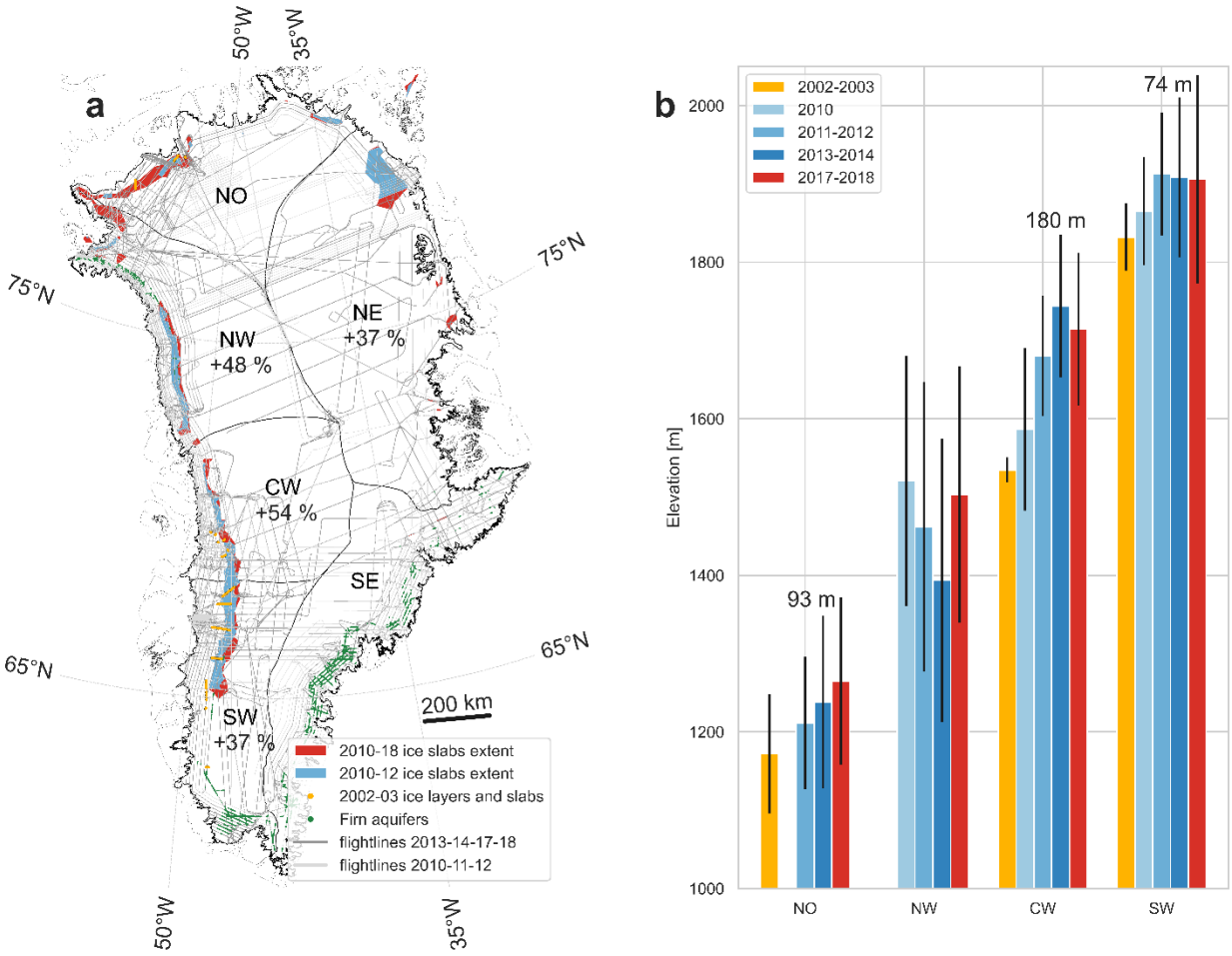

Figure 2. Ice slab extent from 2002 to 2018. (a) Ice layers and slabs in 2002-03 (orange), ice slab extent in 2010-12 (blue) and 2010-18 (red), firn aquifers in 2010-2014 (Miège et al., 2016) (green). Ice slab extents are derived from multiple flight lines (Fig. S8). Flight lines used for identification of 2010-2018 ice slabs (light grey: 2010-12, dark grey: 2013-18). Percentages indicate the upglacier expansion of ice slab extent in 2017-2018 with respect to 2010-12. (b) Maximum ice slab elevation (coloured bars) +/- 1 standard deviation (black bars) in each region. Numbers indicate the change in maximum ice slab elevation between 2002-03 and 2017-18. Elevations are above WGS84 ellipsoid. Maximum elevation changes in the NE, are omitted, as well as extent change in the NO and north of the NW as there was insufficient overlap in flight lines between the different periods (Fig. S7a-e).

Considering the extents of our slab retrievals (Figs. 2a, S8), ice slabs occupied over 60,400-73,500 km^2 (low-high bounds) in 2018, consistent with 2015-2019 ice slabs retrievals extending over 76,000 km^2 using satellite microwave radiometry by Miller et al., (2022). Except in the southern part of SW Greenland, we did not identify any entirely new ice slabs in either 2002-03 or 2017-18 compared to the 2010-14 mapping performed by MacFerrin et al., (2019) (Fig. S8).

We examined inland expansion between 2010-12 and 2017-18 (Fig. 2a). We use 2010-12 because there is good spatial coverage in 2011-12 supported by complementary coverage in 2010 (Fig. S7b-e). We estimate that the ice slab area increased from 2010-12 to 2017-18 by 37% in the NE and the SW, 48% in the NW, and 54% in the CW. We also calculated the maximum ice slab elevation in each period by picking the maximum elevation in 10 km-wide boxes, then calculating the median value in each region. This showed that the increase in area was driven by ice slab expansion to higher elevations throughout the west coast (Figs. 2b, S8), in agreement with the upslope expansion of ice slabs identified by Miller et al., (2022).

3.2 Ice slab thickening

The accumulation radar used between 2010 and 2018 has a vertical resolution of 65 cm in snow and firn (Rodriguez-Morales et al., 2014), enabling the examination of changes in ice slab thickness along repeated radar survey lines. We focus on six transects which had repeated radar surveys within tens to hundreds of metres of each other (Fig. 3) and differentiate between three stages of ice slab change between 2010 and 2018: (i) initiation (i.e. appearance of a ~meter-thick slab), (ii) development (i.e. significant thickening of existing ice slab) and (iii) well-developed (i.e. already at least 10 m thick) (Text S3, Fig. S5). Ice content increased between 2010 and 2018 along all the transects. While there were no major thickness changes where well-developed ice slabs were already present in 2010 (e.g. Fig. 3f from 0 to 23 km), we observed development of thinner ice slabs. On transect A, ice content at 11-13 km increased by 13.5 m between 2011-12 and 2017-18. On transect B, the slab at 8-15 km thickened from less than 2 m in 2010 to roughly 5 m by 2017-18.

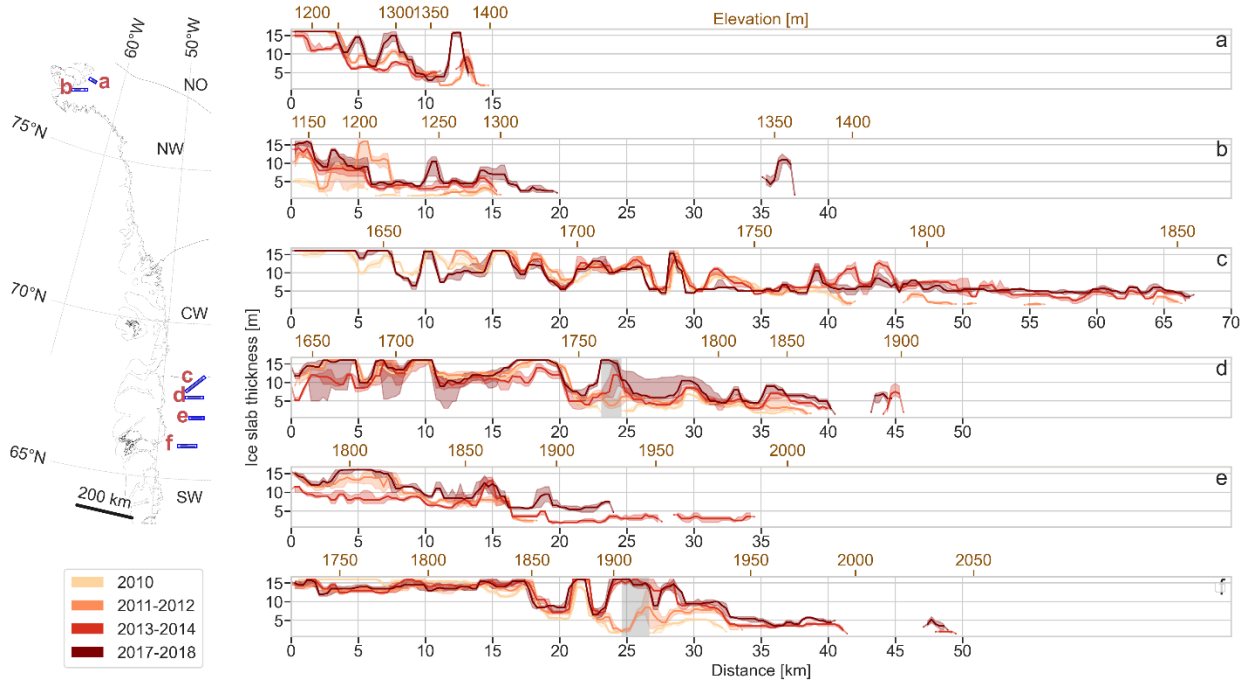

Figure 3. Ice slab thickness over time. Ice thickness derived from our upper ice content detection threshold (quantile 0.79). For each transect, the data were aggregated from the start of the transect into 300 m bins, smoothed with a 900 m rolling median. Median in bold, interquartile range denoted by shading.

Previously discontinuous ice slabs merged laterally over time (Fig. 3b-d,f). On transect C, a 5 to 10 m-thick ice slab developed above the 2010 upper limit (at 41 km) by 2013-14, fusing several previously thinner and isolated areas of ice slab. Consequently, the upper limit of ice slabs expanded inland by 26 km from 2010 to 2017. On transect D (Fig. 3d), the ice-free section in between 23-24.5 km (grey shading) saw initial ice slab generation during summer 2010. This area developed to 16 m by 2018, filling the gap between two previously unconnected slabs and expanding the continuous ice slab by 17.4 km. Similar behaviour is apparent in transect F (Fig. 3f grey shading).

To examine ice slab initiation and thickening in more detail, we examined radargrams along a transect with good repeat radar coverage near to the KAN_U weather station at which meteorological measurements have been made continuously since 2009 (Fig. 4). No radar data were acquired in this area during 2002-03, but radargrams acquired in the nearby area during

2010 and 2011 show sub-surface decimeters to meters-thick ice content (Fig. S9a-b). 2014 and 2017 radargrams are offset by several hundreds of meters from 2012, 2013 and 2018 radargrams (900 m at 13.8 km, 1700 m at 40 km, Fig. 4a). The ice content can vary significantly between non-perfectly overlapping transects. For example, the ice content between 13.8 and 15.6 km is ~59% less in the 2014 retrieval compared to 2013 (Fig. 4b-c). Nonetheless, we still detected overall thickening through time (Figs. 4d, S9h). Between 2012 and 2018, the ice thickened between 0 and 13.8 km (+9%), increased substantially between 13.8 and 17.7 km (+43%), and a new ice slab developed from 18.5 km.

To relate the changes in ice thickness to the potential for meltwater percolation and refreezing, we used total annual Positive Degree Hours (PDH) as a first-order estimate of summer melting (Fig. S6). Following the extreme melt-year of 2012 with 1273 ℃ PDH, ice content between 13.8 and 17.7 km increased by 4,576 m^2 (19 %) from spring 2012 to spring 2013. From summer 2013 to 2017 there were 2233 ℃ PDH – 175% of 2012 – yet ice content increased by only 5,738 m^2 between spring 2013 and spring 2018, equivalent to 25 % more ice content formation than 2012 alone.

We observed that ice slabs can thicken by ice accretion (i) on top of existing ice content versus (ii) beneath. Considering top-down accretion, between 16.5 to 17.7 km there was 2.9 m thickening from above between 2012 and 2018 (Fig. 4d); the bottom of the slab deepened by 3 m with respect to the surface due to gradual burial (Text S4). Directly beneath KAN_U, 0.8 m ice was added to the top of the ice slab due to high PDH in summer 2012 (Fig. 4b), and 0.6 m during summer 2013 (Figs. 4b-c, S9h), even though the 2013 PDH was only 30% of the 2012 PDH (Fig. S6). The subsequent 2.5 m of top-down thickening between 2014 and 2018 occurred during only moderate melting in 2014 and 2016 and limited melting in 2015 and 2017 (Figs. 4c-d, S6, S9e-h). There is further evidence of accretion on top of existing ice slabs in transects C-F (Fig. S10).

Between 13.8 and 15.6 km there was ~4 m of thickening predominantly below the slab between 2012 and 2018 (Fig. 4b,d). This was generated by ~1.5 m of accretion predominantly below the existing ice slab due to summer 2012 (Fig. 4b), and a further ~2.5 m of accretion during 2014-2017 split between thickening from above and below (Figs. 4b,d, S9d,g). We also observed localized accretion below existing ice slabs in transects A, B and E (Fig. S10).

Ice slab expansion to higher elevations predominantly occurred through accretion on top of existing near-surface ice layers. At 2012's upper ice slab boundary (18.5 km), a ~1 m layer grew by spring 2013, subsequently thickening to 6 m by 2018 and yielding 5.7 km of inland slab expansion (Fig. 4d). Conversely, from ~25 km onwards the near-surface ice layer identified in spring 2013 (Fig. 4b) was buried by subsequent accumulation (Fig. 4d).

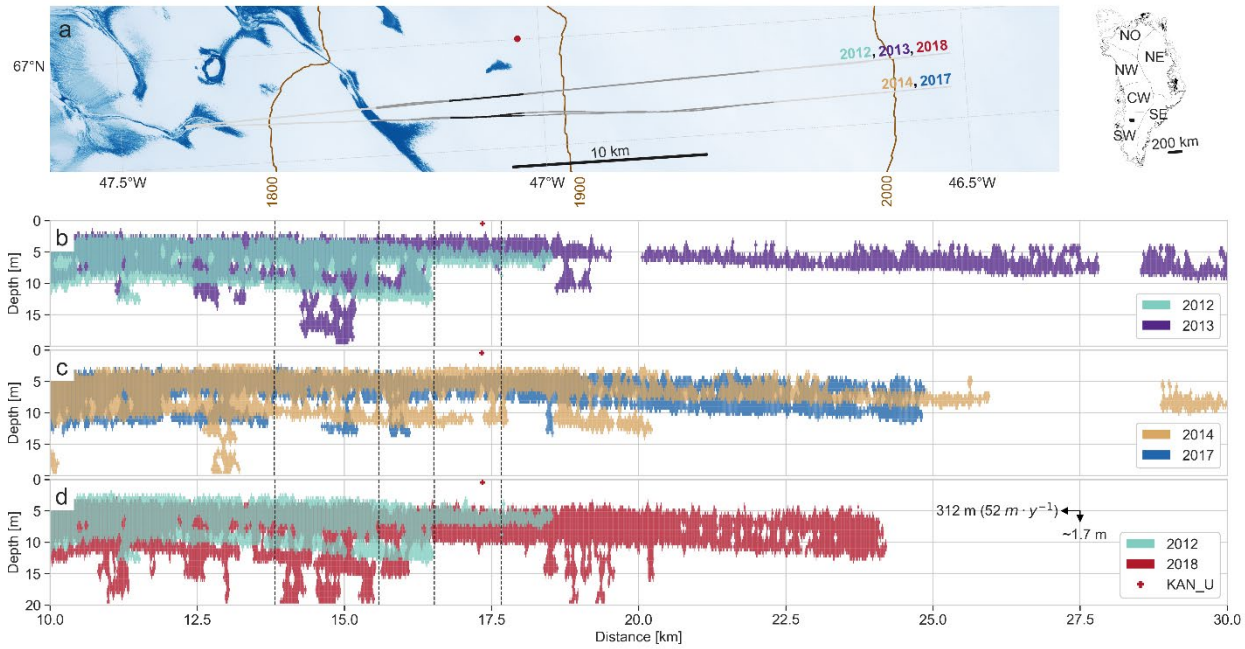

Figure 4. Ice thickness change through time along a transect close to KAN_U. (a) Near-infrared (band 8) Sentinel-2 image acquired on August 23rd, 2021, complete radargram extent (light grey), radargram extent (dark grey) shown in panels b-d, ~4km transect of interest (black), location of KAN_U (red dot). (b-d) Maximum likely ice content between different repeat radargrams. The dashed vertical lines delineate specific areas discussed in the text. In panel d, the vertical arrow illustrates burial from 2013 to 2017 due to firn replenishment; the horizontal arrow illustrates the lateral movement of the ice from 2012 to 2018 (Text S4).

4 Discussion

4.1 Mechanisms of ice slab formation and thickening

We identify three principal mechanisms of ice slab formation and thickening. (i) Meltwater percolation and refreezing generates initial ice layers in porous firn. Then, accretion of ice by meltwater refreezing proceeds (ii) on top of, and/or (iii) beneath pre-existing ice layers.

In the data presented in Fig. 4, mechanism (i) was responsible for the initial generation of a 3 m-thick near-surface contiguous ice slab by the fusing of pre-existing discontinuous ice layers in porous firn from 18.5 km onwards during summer 2012. Culberg et al. (2021) and de la Peña et al. (2015) similarly showed that the initiation of near-surface ice layers can occur within a single extremely warm summer.

Radar observations can differentiate between subsequent thickening by accretion (ii) on top of, and (iii) below existing ice content. We interpret that unexceptional but sustained melting conditions such as in 2014 or 2016 predominantly cause thickening by accretion on top of pre-existing ice slabs (Figs. 4c, S6, S9c-g). Machguth et al., (2016) also evidenced top-down ice accretion due to the 2013 and 2014 moderate melt summers by comparing 2015 and 2013 cores. Hence, once ice slabs form, they thicken even in moderate melt years.

Accretion below existing ice slabs (Fig. 4b,d) was primarily associated with the large PDH sum during summer 2012 (Fig. S6). We propose that abundant meltwater - which may have originated from higher elevations (Clerx et al., 2022) - was able to exploit local areas of higher permeability. Previous observations show that deep percolation (> 10 m) can occur in firn without homogeneous wetting front advance (Humphrey et al., 2012; Machguth et al., 2016; Samimi et al., 2020). However, these processes are less likely to occur through several meters thick ice slabs. In northwest Greenland, Culberg et al., (2022) found that meltwater associated with visible runoff features probably exploits fractures to penetrate through the ice slab and refreeze underneath. We find multiple lines of evidence which support this process further south. First, crevasses have been observed at high elevations in the percolation zone of central-west Greenland (Colgan et al., 2016), providing paths for meltwater to flow vertically. Second, the accretion of ice beneath ice slabs observed downstream of KAN_U (Fig. 4) is associated with meltwater ponding in a slush field (Fig. S11). Third, sudden firn warming at 5 m depth at

KAN_U in September 2012 strongly supports abrupt meltwater penetration through a 3 m thick ice slab, followed by gradual cooling through winter indicative of refreezing (Machguth et al., (2016) Figs. S4 and S5a). Finally, firn cores acquired in 2012 and 2013 show ice accretion at a depth of 5 m in-between existing ice slabs (Machguth et al., (2016) Fig. S4c).

4.2 Changes in sub-surface firn and implications

Immediately above the current ice slab extent in SW Greenland, the firn is primed for further ice slab development. Indeed, cores from Site J (2040 m asl) acquired in 1989 and 2017 clearly show the merging of ice lenses into several ~1 m thick layers in the uppermost 12 m (Rennermalm et al., 2021), and cores acquired at Dye-2 (2,120 m asl) in 1998 and 2013 tell a similar story (Machguth et al., 2016). The increase in firn density and ice content is consistent with recent warmer surface conditions (de la Peña et al., 2015).

Surface melting is projected to increase in the percolation zone (Fettweis et al., 2013; Franco et al., 2013), and extreme summer melting events such as 2010 and 2012 are expected to become more frequent (Bevis et al., 2019). Yet, radargrams indicate that the fate of the near-surface ice layer generated in summer 2012 varied by elevation.

Towards the lower elevations of the ice layer that was mostly generated due to summer 2012 (from 18.5 km onwards), additional ice accreted, forming ice slabs by 2017-18 (Fig. 4). Conversely, at higher elevations where melt was infrequent between 2013 and 2017 (Fig. S6), the near-surface layer generated in 2012 was progressively buried to moderate depths, reducing the likelihood that it will support ice slab growth in the future. The upper limit of the summer 2012 ice layer (Fig. S9d) is located 260 m away from the location of Core 3 (Rennermalm et al., 2021). The later layer probably corresponds to the numerous ice layers found in the uppermost 9 m of Core 3 in 2013. By 2018, these ice layers had been buried and could no longer be identified by radar (Fig. S9e-g), in agreement with ~3.5 m of firn replenishment identified by the redrilling of Core 3 in 2019. This is consistent with Culberg et al. (2021), who showed that the 2012 near-surface melt layer above 2600 m asl in central Greenland was initially located at 1 m deep, and was still present in 2017 but had been buried to a depth of 5 m. Thus, the ability of near-surface ice layers to support subsequent ice slab development is likely to depend on whether strong melting occurs during several successive summers.

Considering recent sub-surface changes between 2013 and 2017, cores at KAN_U (Fig. 6a in Rennermalm et al. (2021)) show that the top of the ice slab was at roughly the same depth in 2017 as 2013. However, the 2015 and 2016 cores showed some evidence of firn replenishment. We suggest that this replenishment subsequently melted during summer 2016 (Fig. S6) and refroze on top of the slab. Thus, the effect of isolated years of firn replenishment, which temporarily bury an ice slab, can be easily erased by relatively moderate melting.

5 Conclusions

We interpreted accumulation radar data to show that ice slabs already existed in 2002-03 in SW, CW and NO Greenland, which are most likely a result of increasing surface melting from the mid-1990s onwards (van As et al., 2016). On an ice-sheet-wide basis we showed that ice slabs expanded inland from 2012 to 2018 by 13,400-17,600 km^2, or 37-44%.

We identified two mechanisms by which ice slabs thicken: wide-spread ice accretion on top of pre-existing ice slabs, and more localised ice accretion beneath pre-existing ice slabs. We suggest that deep percolation through ice slabs takes place beneath ponded surface meltwater features and exploits local fractures in otherwise near-impermeable ice slabs. Accretion below pre-existing ice slabs is therefore more likely during extreme melt seasons, while more moderate melt seasons predominantly result in top-down thickening.

Extremely warm summers such as 2012 can produce enough meltwater at higher elevations to generate a near-surface ice layer on the order of at least a meter thick, forming the basis for subsequent ice slab expansion via top-down ice accretion. Once formed, ice slabs continue to thicken, even under moderate melting conditions.

We suggest that future increases in melting at higher elevations will trigger further ice slab development, increasing the ice slab area non-linearly with elevation because of the non-linearity of the hypsometry of the ice sheet (Bauer, 1955). The recent expansion of the visible runoff area of the Greenland Ice Sheet (Tedstone & Machguth, 2022) is strongly linked with the expansion of ice slabs (Fig. S12), so future increases in ice slab area are likely to further increase the area which contributes runoff to the oceans.

Acknowledgments

This work was funded under the European Research Council award 818994 – CASSANDRA. We acknowledge the use of data and data products from CReSIS generated with support from the University of Kansas, NASA Operation IceBridge grant NNX16AH54G, NASA grant NNX10AT68G, NSF grants ACI-1443054, OPP-1739003, and IIS-1838230, ANT-0424589, Lilly Endowment Incorporated, and the Indiana METACyt Initiative. We thank P. Bednawrek (University of Fribourg) for computational support.

Open Research

2002-2003 and 2010-2018 accumulation radar data (CReSIS, 2021) are available on the CReSIS data repository (https://data.cresis.ku.edu/data/accum/). We used the ArcticDEM digital elevation model at 100m resolution, which provides elevation above the WGS84 ellipsoid (https://www.pgc.umn.edu/data/arcticdem/). The regional divisions of the GrIS are based on the Greenland Ice Sheet drainage basins from Rignot & Mouginot (2012). Air temperatures at the automatic weather station KAN_U station can be downloaded from https://doi.org/10.22008/promice/data/aws. Sentinel 2 satellite images can be downloaded at https://scihub.copernicus.eu/dhus/#/home. The scripts used to perform the analysis for this study can be found at https://github.com/jullienn/changing_Greenland_iceslabs. Our ice slab dataset is available at https://doi.org/10.5281/zenodo.7505426.

Author contributions

NJ, AT and HM designed the study. NK contributed to interpretation of the 2002-03 radargrams. NJ developed the methodology for ice identification in 2010-18 data, with contributions from VH, HM and AT. NJ carried out data processing, data analysis and interpretation. NJ and AT wrote the manuscript based on comments from all co-authors.

References

Bauer, A. (1955). The Balance of the Greenland Ice Sheet. *Journal of Glaciology*, *2*(17), 456–462. Cambridge Core. https://doi.org/10.3189/002214355793702271

Bevis, M., Harig, C., Khan, S. A., Brown, A., Simons, F. J., Willis, M., Fettweis, X., van den Broeke, M. R., Madsen, F. B., Kendrick, E., Caccamise, D. J., van Dam, T., Knudsen, P., & Nylen, T. (2019). Accelerating changes in ice mass within Greenland, and the ice sheet's sensitivity to atmospheric forcing. *Proceedings of the National Academy of Sciences*, *116*(6), 1934–1939. https://doi.org/10.1073/pnas.1806562116

Braithwaite, R. J., Laternser, M., & Pfeffer, W. T. (1994). Variations of near-surface firn density in the lower accumulation area of the Greenland ice sheet, Pâkitsoq, West Greenland. *Journal of Glaciology*, *40*(136), 477–485. Cambridge Core. https://doi.org/10.3189/S002214300001234X

Brown, J., Harper, J., Pfeffer, W. T., Humphrey, N., & Bradford, J. (2011). High-resolution study of layering within the percolation and soaked facies of the Greenland ice sheet. *Annals of Glaciology*, *52*(59), 35–42. https://doi.org/10.3189/172756411799096286

Carl, L., Lewis, C., Gogineni, P., Rodriguez, F., Paden, J., & Li, J. (2011). *IceBridge Accumulation Radar L1B Geolocated Radar Echo Strength Profiles, 2010, 2011, 2012, 2013, 2014, 2017, 2018 [Dataset]*. Boulder, Colorado USA: National Snow and Ice Data Center. Digital media. https://data.cresis.ku.edu/data/accum/.

Clerx, N., Machguth, H., Tedstone, A., Jullien, N., Wever, N., Weingartner, R., & Roessler, O. (2022). *In situ measurements of meltwater flow through snow and firn in the accumulation zone of the SW Greenland Ice Sheet* [Preprint]. Ice sheets/Glacier Hydrology. https://doi.org/10.5194/egusphere-2022-71

Colgan, W., Rajaram, H., Abdalati, W., McCutchan, C., Mottram, R., Moussavi, M. S., & Grigsby, S. (2016). Glacier crevasses: Observations, models, and mass balance implications: Glacier Crevasses. *Reviews of Geophysics*, *54*(1), 119–161. https://doi.org/10.1002/2015RG000504

CReSIS. (2021). *Accumulation radar Data, 2002, 2003, 2010, 2011, 2012, 2013, 2014, 2017, 2018 [Dataset] Lawrence, Kansas, USA. Digital Media.* http://data.cresis.ku.edu/

Culberg, R., Chu, W., & Schroeder, D. M. (2022). Shallow Fracture Buffers High Elevation Runoff in Northwest Greenland. *Geophysical Research Letters*, *49*(23). https://doi.org/10.1029/2022GL101151

Culberg, R., Schroeder, D. M., & Chu, W. (2021). Extreme melt season ice layers reduce firn permeability across Greenland. *Nature Communications*, *12*(1), 2336. https://doi.org/10.1038/s41467-021-22656-5

de la Peña, S., Howat, I. M., Nienow, P. W., van den Broeke, M. R., Mosley-Thompson, E., Price, S. F., Mair, D., Noël, B., & Sole, A. J. (2015). Changes in the firn structure of the western Greenland Ice Sheet caused by recent warming. *The Cryosphere*, *9*(3), 1203–1211. https://doi.org/10.5194/tc-9-1203-2015

Enderlin, E. M., Howat, I. M., Jeong, S., Noh, M.-J., van Angelen, J. H., & van den Broeke, M. R. (2014). An improved mass budget for the Greenland ice sheet. *Geophysical Research Letters*, *41*(3), 866–872. https://doi.org/10.1002/2013GL059010

Fausto, R. S., van As, D., Mankoff, K. D., Vandecrux, B., Citterio, M., Ahlstrøm, A. P., Andersen, S. B., Colgan, W., Karlsson, N. B., Kjeldsen, K. K., Korsgaard, N. J., Larsen, S. H., Nielsen, S., Pedersen, A. Ø., Shields, C. L., Solgaard, A. M., & Box, J. E. (2021). *Programme for Monitoring of the Greenland Ice Sheet (PROMICE) automatic weather station data*. 27.

Fettweis, X., Box, J. E., Agosta, C., Amory, C., Kittel, C., Lang, C., van As, D., Machguth, H., & Gallée, H. (2017). Reconstructions of the 1900–2015 Greenland ice sheet surface mass balance using the regional climate MAR model. *The Cryosphere*, 19.

Fettweis, X., Franco, B., Tedesco, M., van Angelen, J. H., & Lenaerts, J. T. M. (2013). Estimating the Greenland ice sheet surface mass balance contribution to future sea level rise using the regional atmospheric climate model MAR. *The Cryosphere*, 21.

Fettweis, X., Hofer, S., Krebs-Kanzow, U., Amory, C., Aoki, T., Berends, C. J., Born, A., Box, J. E., Delhasse, A., Fujita, K., Gierz, P., Goelzer, H., Hanna, E., Hashimoto, A., Huybrechts, P., Kapsch, M.-L., King, M. D., Kittel, C., Lang, C., … Tedesco, M. (2020). GrSMBMIP: intercomparison of the modelled 1980–2012 surface mass balance over the Greenland Ice Sheet. *The Cryosphere*, 24.

Forster, R. R., Box, J. E., van den Broeke, M. R., Miège, C., Burgess, E. W., van Angelen, J. H., Lenaerts, J. T. M., Koenig, L. S., Paden, J., Lewis, C., Gogineni, S. P., Leuschen, C., & McConnell, J. R. (2014). Extensive liquid meltwater storage in firn within the Greenland ice sheet. *Nature Geoscience*, *7*(2), 95–98. https://doi.org/10.1038/ngeo2043

Franco, B., Fettweis, X., & Erpicum, M. (2013). Future projections of the Greenland ice sheet energy balance driving the surface melt. *The Cryosphere*, *7*(1), 1–18. https://doi.org/10.5194/tc-7-1-2013

Hall, D. K., Comiso, J. C., DiGirolamo, N. E., Shuman, C. A., Box, J. E., & Koenig, L. S. (2013). Variability in the surface temperature and melt extent of the Greenland ice sheet from MODIS: TEMPERATURE AND MELT OF GREENLAND ICE. *Geophysical Research Letters*, *40*(10), 2114–2120. https://doi.org/10.1002/grl.50240

Harper, J., Humphrey, N., Pfeffer, W. T., Brown, J., & Fettweis, X. (2012). Greenland ice-sheet contribution to sea-level rise buffered by meltwater storage in firn. *Nature*, *491*(7423), 240–243. https://doi.org/10.1038/nature11566

Hock, R. (2003). Temperature index melt modelling in mountain areas. *Journal of Hydrology*, *282*(1–4), 104–115. https://doi.org/10.1016/S0022-1694(03)00257-9

Humphrey, N. F., Harper, J. T., & Pfeffer, W. T. (2012). Thermal tracking of meltwater retention in Greenland's accumulation area: THERMAL TRACKING OF MELTWATER RETENTION. *Journal of Geophysical Research: Earth Surface*, *117*(F1), n/a-n/a. https://doi.org/10.1029/2011JF002083

Kanagaratnam, P., Gogineni, S. P., Ramasami, V., & Braaten, D. (2004). A Wideband Radar for High-Resolution Mapping of Near-Surface Internal Layers in Glacial Ice. *IEEE Transactions on Geoscience and Remote Sensing*, *42*(3), 483–490. https://doi.org/10.1109/TGRS.2004.823451

Karlsson, N. B., Colgan, W. T., Binder, D., Machguth, H., Abermann, J., Hansen, K., & Pedersen, A. Ø. (2019). Ice-penetrating radar survey of the subsurface debris field at Camp Century, Greenland. *Cold Regions Science and Technology*, *165*, 102788. https://doi.org/10.1016/j.coldregions.2019.102788

King, M. D., Howat, I. M., Candela, S. G., Noh, M. J., Jeong, S., Noël, B. P. Y., van den Broeke, M. R., Wouters, B., & Negrete, A. (2020). Dynamic ice loss from the Greenland Ice Sheet driven by sustained glacier retreat. *Communications Earth & Environment*, *1*(1), 1. https://doi.org/10.1038/s43247-020-0001-2

Lewis, C. (2010). *Airborne UHF Radar for Fine Resolution Mapping of Near-Surface Accumulation Layers in Greenland and West Antarctica, (Master's thesis)* [University of Kansas]. Retrieved from KU Scholar Works data repository (http://hdl.handle.net/1808/7008)

MacFerrin, M., Machguth, H., As, D. van, Charalampidis, C., Stevens, C. M., Heilig, A., Vandecrux, B., Langen, P. L., Mottram, R., Fettweis, X., Broeke, M. R. van den, Pfeffer, W. T., Moussavi, M. S., & Abdalati, W. (2019). Rapid expansion of Greenland's low-permeability ice slabs. *Nature*, *573*(7774), 403–407. https://doi.org/10.1038/s41586-019-1550-3

Machguth, H., MacFerrin, M., van As, D., Box, J. E., Charalampidis, C., Colgan, W., Fausto, R. S., Meijer, H. A. J., Mosley-Thompson, E., & van de Wal, R. S. W. (2016). Greenland meltwater storage in firn limited by near-surface ice formation. *Nature Climate Change*, *6*(4), 390–393. https://doi.org/10.1038/nclimate2899

Miège, C., Forster, R. R., Brucker, L., Koenig, L. S., Solomon, D. K., Paden, J. D., Box, J. E., Burgess, E. W., Miller, J. Z., McNerney, L., Brautigam, N., Fausto, R. S., & Gogineni, S. (2016). Spatial extent and temporal variability of Greenland firn aquifers detected by ground and airborne radars. *Journal of Geophysical Research: Earth Surface*, *121*(12), 2381–2398. https://doi.org/10.1002/2016JF003869

Mikkelsen, A. B., Hubbard, A., MacFerrin, M., Box, J. E., Doyle, S. H., Fitzpatrick, A., Hasholt, B., Bailey, H. L., Lindbäck, K., & Pettersson, R. (2016). Extraordinary runoff from the Greenland ice sheet in 2012 amplified by hypsometry and depleted firn retention. *The Cryosphere*, *10*(3), 1147–1159. https://doi.org/10.5194/tc-10-1147-2016

Miller, J. Z., Culberg, R., Long, D. G., Shuman, C. A., Schroeder, D. M., & Brodzik, M. J. (2022). An empirical algorithm to map perennial firn aquifers and ice slabs within the Greenland Ice Sheet using satellite L-band microwave radiometry. *The Cryosphere*, *16*(1), 103–125. https://doi.org/10.5194/tc-16-103-2022

Nghiem, S. V., Hall, D. K., Mote, T. L., Tedesco, M., Albert, M. R., Keegan, K., Shuman, C. A., DiGirolamo, N. E., & Neumann, G. (2012). The extreme melt across the Greenland ice sheet in 2012. *Geophysical Research Letters*, *39*(20), 2012GL053611. https://doi.org/10.1029/2012GL053611

Pfeffer, W. T., & Humphrey, N. F. (1998). Formation of ice layers by infiltration and refreezing of meltwater. *Annals of Glaciology*, *26*, 83–91. https://doi.org/10.3189/1998AoG26-1-83-91

Pfeffer, W. T., Meier, M. F., & Illangasekare, T. H. (1991). Retention of Greenland runoff by refreezing: Implications for projected future sea level change. *Journal of Geophysical Research*, *96*(C12), 22117. https://doi.org/10.1029/91JC02502

Rennermalm, Å. K., Hock, R., Covi, F., Xiao, J., Corti, G., Kingslake, J., Leidman, S. Z., Miège, C., Macferrin, M., Machguth, H., Osterberg, E., Kameda, T., & McConnell, J. R. (2021). Shallow firn cores 1989–2019 in southwest Greenland's percolation zone reveal decreasing density and ice layer thickness after 2012. *Journal of Glaciology*, *68*(269), 431–442. https://doi.org/10.1017/jog.2021.102

Rignot, E., Box, J. E., Burgess, E., & Hanna, E. (2008). Mass balance of the Greenland ice sheet from 1958 to 2007. *Geophysical Research Letters*, *35*(20), L20502. https://doi.org/10.1029/2008GL035417

Rignot, E., & Mouginot, J. (2012). Ice flow in Greenland for the International Polar Year 2008-2009: ICE FLOW GREENLAND 2009. *Geophysical Research Letters*, *39*(11), n/a-n/a. https://doi.org/10.1029/2012GL051634

Rodriguez-Morales, F., Byers, K., Crowe, R., Player, K., Hale, R. D., Arnold, E. J., Smith, L., Gifford, C. M., Braaten, D., Panton, C., Gogineni, S., Leuschen, C. J., Paden, J. D., Li, J., Lewis, C. C., Panzer, B., Gomez-Garcia Alvestegui, D., & Patel, A. (2014). Advanced Multifrequency Radar Instrumentation for Polar Research. *IEEE Transactions on Geoscience and Remote Sensing*, *52*(5), 2824–2842. https://doi.org/10.1109/TGRS.2013.2266415

Rodriguez-Morales, F., Gogineni, P., Leuschen, C., Allen, C., Lewis, C., Patel, A., Byers, K., Smith, L., Shi, L., Panzer, B., Blake, W., Crowe, R., & Gifford, C. (2010). Development of a multi-frequency airborne radar instrumentation package for ice sheet mapping and imaging. *2010 IEEE MTT-S International Microwave Symposium*, 157–160. https://doi.org/10.1109/MWSYM.2010.5518197

455 Samimi, S., Marshall, S. J., & MacFerrin, M. (2020). Meltwater Penetration Through Temperate Ice Layers in the
456 Percolation Zone at DYE-2, Greenland Ice Sheet. *Geophysical Research Letters*, *47*(15).
457 https://doi.org/10.1029/2020GL089211
458 Tedesco, M., & Fettweis, X. (2020). Unprecedented atmospheric conditions (1948–2019) drive the 2019 exceptional
459 melting season over the Greenland ice sheet. *The Cryosphere*, *14*(4), 1209–1223. https://doi.org/10.5194/tc-14-
460 1209-2020
461 Tedesco, M., Fettweis, X., Mote, T., Wahr, J., Alexander, P., Box, J. E., & Wouters, B. (2013). Evidence and
462 analysis of 2012 Greenland records from spaceborne observations, a regional climate model and reanalysis data. *The*
463 *Cryosphere*, *7*(2), 615–630. https://doi.org/10.5194/tc-7-615-2013
464 Tedesco, M., Fettweis, X., van den Broeke, M. R., van de Wal, R. S. W., Smeets, C. J. P. P., van de Berg, W. J.,
465 Serreze, M. C., & Box, J. E. (2011). The role of albedo and accumulation in the 2010 melting record in Greenland.
466 *Environmental Research Letters*, *6*(1), 014005. https://doi.org/10.1088/1748-9326/6/1/014005
467 Tedstone, A. J., & Machguth, H. (2022). Increasing surface runoff from Greenland's firn areas. *Nature Climate*
468 *Change*. https://doi.org/10.1038/s41558-022-01371-z
469 The IMBIE Team. (2020). Mass balance of the Greenland Ice Sheet from 1992 to 2018. *Nature*, *579*(7798), 233–
470 239. https://doi.org/10.1038/s41586-019-1855-2
471 van Angelen, J. H., van den Broeke, M. R., Wouters, B., & Lenaerts, J. T. M. (2014). Contemporary (1960–2012)
472 Evolution of the Climate and Surface Mass Balance of the Greenland Ice Sheet. *Surveys in Geophysics*, *35*(5),
473 1155–1174. https://doi.org/10.1007/s10712-013-9261-z
474 van As, D., Fausto, R. S., Cappelen, J., van de Wa, R. S. W. l, Braithwaite, R. J., Machguth, H., & PROMICE
475 project team, *. (2016). Placing Greenland ice sheet ablation measurements in a multi-decadal context. *GEUS*
476 *Bulletin*, *35*, 71–74. https://doi.org/10.34194/geusb.v35.4942
477 van den Broeke, M. R., Enderlin, E. M., Howat, I. M., Kuipers Munneke, P., Noël, B. P. Y., van de Berg, W. J., van
478 Meijgaard, E., & Wouters, B. (2016). On the recent contribution of the Greenland ice sheet to sea level change. *The*
479 *Cryosphere*, *10*(5), 1933–1946. https://doi.org/10.5194/tc-10-1933-2016
480 Vandecrux, B., MacFerrin, M., Machguth, H., Colgan, W. T., van As, D., Heilig, A., Stevens, C. M., Charalampidis,
481 C., Fausto, R. S., Morris, E. M., Mosley-Thompson, E., Koenig, L., Montgomery, L. N., Miège, C., Simonsen, S. B.,
482 Ingeman-Nielsen, T., & Box, J. E. (2019). Firn data compilation reveals widespread decrease of firn air content in
483 western Greenland. *The Cryosphere*, *13*(3), 845–859. https://doi.org/10.5194/tc-13-845-2019

484